

X- AND GAMMA-RAY LINE EMISSION PROCESSES

V. Tatischeff¹

Abstract. This chapter is intended to provide a general presentation of the atomic and nuclear processes responsible for X-ray line and gamma-ray line emission in various astrophysical environments. I consider line production from hot plasmas, from accelerated particle interactions, from the decay of radioactive nuclei synthesized in stars and from positron annihilation. Spectroscopic properties of these emissions are discussed in the light of the detection capabilities of modern space instruments.

1 Introduction

X- and gamma-ray emission lines are valuable signatures of various high-energy processes at work in the universe, including heating of astrophysical gas to very high temperatures, particle acceleration and nucleosynthesis. Perhaps the most important realization of pioneering high-energy astronomy was that hot plasmas are found essentially everywhere in the universe. More and more detailed observations of thermal X-ray lines provide detailed and often unique information on a wide variety of astrophysical sites, including stellar environments, supernova explosions, accreting compact objects, interstellar and intergalactic media and active galactic nuclei.

Particle acceleration is believed to occur in most of these sites. Our understanding of acceleration mechanisms should greatly benefit from the detection of lines produced through atomic and nuclear interactions of energetic particles with ambient matter. The sun provides valuable examples of these nonthermal radiation processes. The study of nuclear de-excitation lines produced in solar flares has now become a proper domain of solar physics.

Gamma-ray lines are also emitted in the decay of radioactive nuclei. Measurements of gamma-ray activities from cosmic radionuclides testify to the ongoing synthesis of chemical elements and their isotopes in the Galaxy and beyond. These

¹ Centre de Spectrométrie Nucléaire et de Spectrométrie de Masse, IN2P3-CNRS, 91405 Orsay, France

observations are now cornerstones for models of nucleosynthesis in novae, supernovae and stellar interiors.

Positron-electron annihilation radiation is relevant to almost all of high-energy astrophysics. Positrons can be produced by various pair-creation processes in relativistic plasmas, by accelerated particle interactions and by the β^+ -decay of radioisotopes. Observations of their annihilations offer a unique vision of high-energy accreting sources, nucleosynthesis sites and the global structure of the Milky Way.

The aim of this text is to present the physical processes responsible for these various line emissions. I also consider emission processes which have not been observed with assurance yet: X-ray line production from accelerated particle interactions and from the decay of cosmic radioactivities, and gamma-ray line emission from thermonuclear plasmas. However, given the advent of new X-ray and gamma-ray satellites with unprecedented sensitivities and spectral resolutions (see Barret and Knödlseher, this volume), I am optimistic that at least some of these emissions could be detected in the near future.

The scope of this review is restricted to emission lines. In particular, I do not discuss X-ray absorption lines recently observed from a handful of active galactic nuclei, as well as cyclotron absorption features in intense magnetic fields, detected from several X-ray binaries. Nor do I treat the high-energy gamma-ray emission from pion decay.

The plan of this review is the following: in section § 2, I present the basic processes of X-ray line emission in both thermally ionized and photoionized plasmas; in § 3, I consider nonthermal X-ray line production in interactions of accelerated electrons and ions with ambient gas; in § 4, I deal with gamma-ray line emission from nuclear collisions and discuss thermonuclear reactions as well as accelerated ion interactions; in § 5, I consider both the gamma-ray lines and the X-ray lines emitted by the decay of radioactive nuclei synthesized in stars; finally, positron annihilation radiation is discussed in § 6.

2 X-ray line emission from hot plasmas

Thermal X-ray emission is observed from a great variety of sources in the universe (see, e.g., *Astronomy & Astrophysics*, volume 365, for an overview of the recent *XMM-Newton* observations). It is produced in various ion-electron plasmas, which can be first classified as a function of their optical depth in the X-ray energy range ($0.1 \leq E_X \leq 100$ keV):

$$\tau \equiv \tau(E_X) = \alpha(E_X) \times D , \quad (2.1)$$

where $\alpha(E_X)$ is the linear absorption coefficient (in c.g.s. units of cm^{-1}) at photon energy E_X and D is the typical dimension of the emitting plasma (cm)¹. Optically thick sources ($\tau \gg 1$) such as isolated neutron stars essentially emit

¹ $\alpha(E_X)$ is also called the *extinction coefficient* when it includes Compton scattering of the X-rays against the free electrons (e.g. Rybicki & Lightman 1979).

blackbody radiation, with some possible discrete spectral structures due to complicated radiation transfer effects (e.g. Rajagopal & Romani 1996). Optically thin sources include stellar coronæ, supernova remnants, superbubbles, the hot interstellar medium, clusters of galaxies and the intergalactic medium. The emission properties of such sources are usually discussed in terms of the *coronal model*, based on the pioneering attempt of Elwert (1952) to explain the X-ray emission of the solar corona. In this model, the plasma radiation is essentially due to collisions of thermal electrons with ions, but the mechanism for heating the electrons to temperature T_e typically $> 10^6$ K is not specified, i.e. T_e is an external parameter of the model.

Different X-ray emitting plasmas are found in astrophysical objects such as X-ray binaries and active galactic nuclei, in which a nebular gas of relatively high density can be strongly illuminated by the compact X-ray source. The physical state and radiation of such photoionized plasmas are generally assumed to be primarily controlled by the emission of the compact source and are usually described in terms of the *nebular model*, which owes its name to the resemblance of these objects with planetary nebulae. In this section, I briefly present the X-ray line production in the coronal model (§ 2.1) and in the nebular model (§ 2.2) and then discuss some diagnostics of plasma parameters based on high-resolution, X-ray line spectroscopy (§ 2.3).

2.1 Thermally ionized plasmas: the coronal model

The coronal model (see Mewe 1999 for a comprehensive description) applies to an optically thin, tenuous, thermal plasma, in which (i) the electrons and the ions are relaxed to Maxwellian energy distributions, (ii) the ions are essentially in their ground state, i.e. excited state configurations can generally be neglected for the calculation of the ionization balance and (iii) each X-ray photon emitted in a microscopic process does not further interact with the ambient ions and electrons. First order deviations from the coronal model are discussed in Raymond (1988).

2.1.1 Ionization structure

The ionization structure of each element of chemical symbol Z and atomic (proton) number z is generally obtained by solving a set of $z+1$ coupled equations:

$$\frac{1}{n_e} \frac{d\eta_Z^i}{dt} = \eta_Z^{i-1} C_{Z^{+(i-1)}} + \eta_Z^{i+1} \alpha_{Z^{+(i+1)}} - \eta_Z^i (C_{Z^{+i}} + \alpha_{Z^{+i}}), \quad (2.2)$$

where η_Z^i is the ionic fraction of ion Z^{+i} ($\sum_{i=0}^z \eta_Z^i = 1$), $C_{Z^{+i}}$ and $\alpha_{Z^{+i}}$ (in c.g.s. units of $\text{cm}^3 \text{s}^{-1}$) are the total ionization ($Z^{+i} \rightarrow Z^{+(i+1)}$) and total recombination ($Z^{+i} \rightarrow Z^{+(i-1)}$) rate coefficients, respectively, and n_e is the electron density (cm^{-3}). Note that the above equation is valid only if multiple ionizations can be neglected. If the ionization balance is in a steady-state equilibrium ($d\eta_Z^i/dt=0$), the ionization structure of element Z is simply given by a set of equations con-

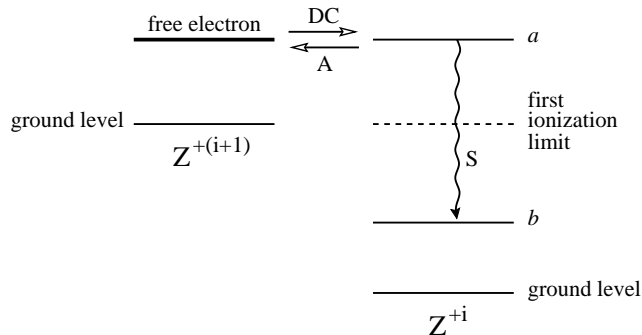


Fig. 1. Scheme of the dielectronic recombination process: a dielectronic capture (DC) into a doubly-excited state a , followed by a stabilizing radiative transition (S) which can produce a satellite line (see text). A: Autoionization.

necting pairs of adjacent ionization states:

$$\eta_Z^i C_{Z^{+i}} = \eta_Z^{i+1} \alpha_{Z^{+(i+1)}} . \quad (2.3)$$

The plasma is said to be at coronal equilibrium when all elements are at ionization equilibrium.

Ionizations are induced by thermal electron collisions. The ionization coefficient $C_{Z^{+i}}$ is obtained by averaging the collisional ionization cross section $\sigma_{Z^{+i}}^I(v)$ over the Maxwell-Boltzmann distribution $f(v)$ of the relative collision velocity, which is generally very close to the velocity distribution of the much lighter electrons:

$$C_{Z^{+i}} = \langle \sigma_{Z^{+i}}^I(v) v \rangle = \int_0^\infty v \sigma_{Z^{+i}}^I(v) f(v) dv , \quad (2.4)$$

with

$$f(v) = \left(\frac{2}{\pi}\right)^{1/2} \left(\frac{m_e}{kT_e}\right)^{3/2} v^2 \exp\left[-\frac{m_e v^2}{2kT_e}\right] , \quad (2.5)$$

where m_e and T_e are the electron mass and temperature and k is the Boltzmann constant. The ionization cross sections are estimated from laboratory measurements combined with atomic physics theory (in particular distorted wave calculations, e.g. Younger 1982 and references therein).

Apart from direct ionization ($Z^{+i} + e^- \rightarrow Z^{+(i+1)} + 2e^-$), ion Z^{+i} can be stripped of one bound electron through the two-step process of excitation-autoionization ($Z^{+i} + e^- \rightarrow (Z^{+i})^* + e^- \rightarrow Z^{+(i+1)} + 2e^-$), which is due to the collisional excitation of an *inner-shell* electron to a bound level above the first ionization threshold, followed by autoionization. The latter process is due to electron-electron interactions, which can break the compound excited state $(Z^{+i})^*$ into its two components: ion $Z^{+(i+1)}$ and a free electron. The contribution of excitation-autoionization to the total ionization cross section is calculated from the sum over all possible autoionizing levels a of the collisional excitation cross sections $\sigma_{Z^{+i}}^{E,a}$, weighted by the autoionization probability of each excited state.

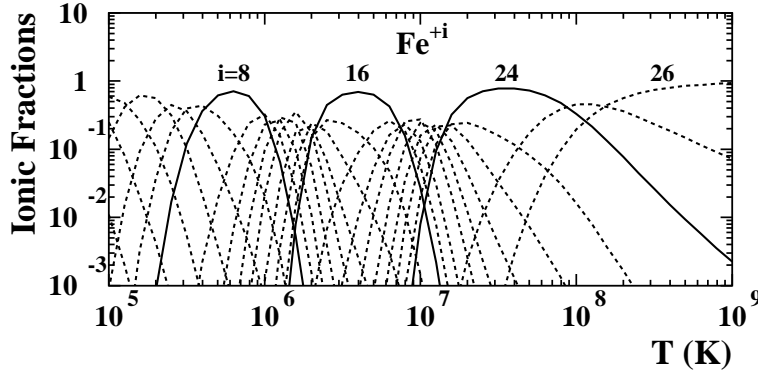


Fig. 2. Iron ionic fractions at ionization equilibrium as a function of plasma temperature (from Arnaud & Raymond 1992).

Recombination of a free electron can proceed either through a radiative free-bound transition ($Z^{+(i+1)} + e^- \rightarrow Z^{+i} + h\nu$) or by a radiationless dielectronic recombination (DR). Charge-transfer reactions are generally negligible for the hot plasmas considered in the coronal model, but can be very important for photoionized plasmas (§ 2.2). Since radiative recombination (RR) is the inverse of photoionization, the rates of the two processes are connected through the principle of time-reversal invariance. The application of this principle by means of the detailed balance theorem leads to the Milne equation (Milne 1924), which is generally used to calculate RR rate coefficients from photoionization data (an example of the use of the Milne equation is provided in § 2.2.2).

However, DR is often the dominant recombination process (e.g. Arnaud & Rothenflug 1985). It is schematically represented in Figure 1. The first step is a dielectronic capture (DC), in which the energy lost by the plasma electron is expended in the simultaneous excitation of one of the bound electrons in the core of the recombining ion $Z^{+(i+1)}$. The atomic level a thus produced is said to be doubly-excited, because its configuration involves two electrons occupying subshells above those which they would occupy in the ground state configuration of ion Z^{+i} . DC is the inverse of autoionization, so that the DC rates can be calculated from the autoionization rates, by applying the principle of detailed balancing. DR occurs if, instead of autoionizing, the doubly-excited state decays by a radiative transition to a level b below the first ionization limit (Fig. 1). The stabilizing decay of the core electron produces a so-called *satellite line*, as it is slightly shifted, usually to the long-wavelength side of the corresponding transition in ion $Z^{+(i+1)}$, due to the electrostatic shielding induced by the spectator outer electron. Satellite line emission can provide very powerful diagnostics of plasma parameters (§ 2.3).

Shown in Figure 2 are the results of Arnaud & Raymond (1992) for the ionic fractions of Fe at ionization equilibrium. We see that ions with closed-shell configurations are more stable than those with partially filled L or M shells. Thus,

He-like Fe XXV (Fe^{+24}), Ne-like Fe XVII (Fe^{+16}) and Ar-like Fe IX (Fe^{+8}), whose ground state configurations are $1s^2$, $2s^22p^6$ and $3s^23p^6$ respectively, are dominant in large temperature ranges, because their ionization and DR rates are relatively low compared to those of adjacent ions.

2.1.2 Line emission

In the coronal model, the line spectrum is dominated by radiative decays following electron impact excitation, plus a smaller contribution of recombination lines. Collisional inner-shell ionization can however be important for plasma diagnostics based on fine spectroscopic analyses (§ 2.3). Considering only the dominant process of collisional excitation, the volume emissivity $P_{Z^{+i}}^{ab}$ (in units of photons $\text{cm}^{-3} \text{s}^{-1}$) of a particular line transition $a \rightarrow b$ in ion Z^{+i} can be written as

$$P_{Z^{+i}}^{ab} = n_e n_H a_Z \eta_Z^i S_{Z^{+i}}^{ga} B_{ab} . \quad (2.6)$$

Here, n_H is the H atomic number density (cm^{-3}), a_Z is the abundance of element Z relative to H, $S_{Z^{+i}}^{ga}$ ($\text{cm}^3 \text{s}^{-1}$) is the rate coefficient for electron impact excitation of ion Z^{+i} from its ground state to its excited state a and B_{ab} is the radiative branching ratio of the transition $a \rightarrow b$ among all possible transitions from level a :

$$B_{ab} = \frac{A_{ab}}{\sum_{c < a} A_{ac}} , \quad (2.7)$$

where A_{ab} is the transition probability (s^{-1}) of the spontaneous decay $a \rightarrow b$ (collisional de-excitation is generally neglected). The excitation rate coefficients $S_{Z^{+i}}^{ga}$ are calculated by averaging the corresponding cross sections over the Maxwellian electron velocity distribution (see eq. 2.4). Semi-empirical fitting formulae have been derived for the most significant exciting transitions in all relevant ions (Mewe 1999 and references therein).

The line spectrum is generally dominated by the “allowed” electric dipole ($E1$) transitions². However, forbidden lines can be relatively bright if they are produced by the decays of excited levels which cannot de-excite by an $E1$ transition. With the advent of new X-ray instruments with high sensitivity and resolution capabilities, such as those aboard the *XMM-Newton* and *Chandra* satellites, the correct modeling of relatively weak lines has become increasingly important. The three main coronal-plasma emission codes, SPEX (Kaastra *et al.* 1996), CHIANTI

² In the Russell-Saunders LS -coupling, which generally holds for the most abundant ions (i.e. whose atomic number $z < 29$), the quantum selection rules of the $E1$ transitions are (e.g. Sobelman 1979): $\Delta J = J_a - J_b = 0$ or ± 1 , with $J_a + J_b \geq 1$; $\Delta M = M_{J_a} - M_{J_b} = 0$ or ± 1 ; $\Delta L = L_a - L_b = 0$ or ± 1 , with $L_a + L_b \geq 1$; $\Delta S = S_a - S_b = 0$; $\pi_a = -\pi_b$; and $\Delta \ell = \ell - \ell' = \pm 1$. Here, L_a and S_a are the orbital and spin angular momenta of the atomic energy level a , which combine to the total angular momentum J_a of magnetic quantum number M_{J_a} ; π_a is the parity of level a ; and ℓ and ℓ' are the orbital angular momenta of the individual “jumping” electron in the atomic states a and b , respectively. Radiative transitions which violate one of these selection rules are said to be “forbidden” and are usually weaker.

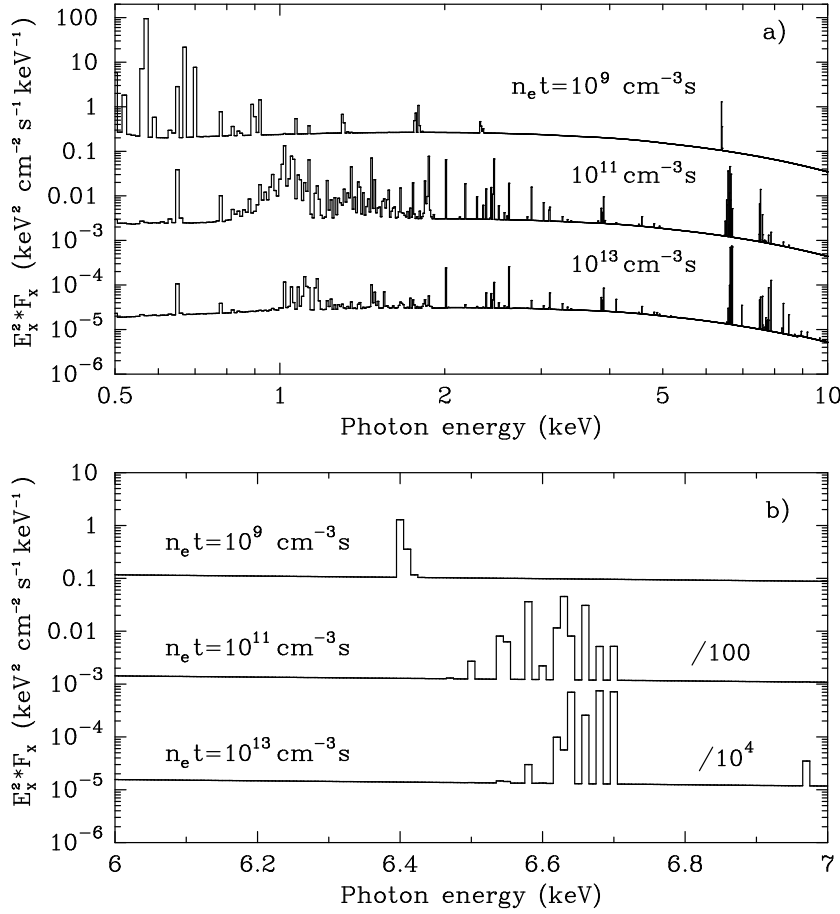


Fig. 3. Thermal X-ray emissions between 0.5 and 10 keV (panel *a*) and around the Fe K line complex (panel *b*) of an optically thin transient plasma with solar abundances and electron temperature $T_e=30$ MK, for three values of the ionization parameter. For $n_e t=10^{13} \text{ cm}^{-3} \text{ s}$, the plasma has reached the ionization equilibrium. The calculations are normalized to the reduced emission measure $EM/(4\pi D^2)=10^{14} \text{ cm}^{-5}$, where D is the distance to the source and $EM = \int n_e n_H dV$ (in cm^{-3}) is the total emission measure (which is directly proportional to the X-ray production rate, see eq. 2.6). In each panel, the spectra for $n_e t=10^{11}$ and $10^{13} \text{ cm}^{-3} \text{ s}$ are divided by 100 and 10^4 , respectively. All spectra are plotted in energy bins of 10 eV.

(Landi *et al.* 1999) and APEC (Smith *et al.* 2001), now calculate tens of thousands of lines in the X-ray energy band.

As an illustration of the dependence of the X-ray line spectrum on the ioniza-

tion structure of a radiating plasma, Figure 3 shows calculated emissions of a transient source, that has been instantaneously heated to $T_e=30\times 10^6$ K at time $t=0$. I used the non-equilibrium ionization (NEI) plasma model (Borkowski *et al.* 2001 and references therein), recently implemented in the XSPEC v11 spectral software package (see Ballet, this volume). Assuming constant electron temperature and density, we see from eq. (2.2) that the evolution of the ionization structure can be entirely characterized by the product $n_e t$, which is called the ionization parameter. The evolving line spectrum is superimposed on a quasi-static continuum, which, for $T_e=30$ MK, is mainly produced by the thermal bremsstrahlung of the plasma electrons (free-free emission). However, the continuum radiation of plasmas with lower temperatures is often dominated by radiative recombinations (Mewe *et al.* 1986). This emission is considered in § 2.2.2.

The line emission generally shifts towards higher energies as the emitting ions become more and more ionized. For example, we see for $n_e t=10^{11}$ cm⁻³ s in panel (a), a prominent line forest at ~ 1 keV, which mainly consists of Fe L lines, i.e. $3\ell\rightarrow 2\ell'$ electronic transitions in ions Fe XVII-XXIV. This emission is much weaker for $n_e t=10^{13}$ cm⁻³ s, because in a 30 MK plasma at ionization equilibrium the most abundant Fe ion is the He-like Fe XXV (see Fig. 2). The strongest line emission is then the Fe K α line complex ($2p\rightarrow 1s$ transitions in the Siegbahn notation) at ~ 6.7 keV. Fe K lines are also produced by inner-shell excitation or ionization of less ionized Fe, but as shown in panel (b), their energies are slightly lower, because the atomic levels get closer as the electrostatic shielding induced by the bound electrons increases. For example, the Fe K α line (which is made of the two very close components $K\alpha_1\equiv 2p_{3/2}\rightarrow 1s_{1/2}$ and $K\alpha_2\equiv 2p_{1/2}\rightarrow 1s_{1/2}$) is at 6.40 keV for Fe II-XII, 6.70 keV for Fe XXV and 6.97 keV for Fe XXVI (see panel b). Determinations of the precise energy and intensity of various lines thus provide direct information on the ionization structure of a coronal plasma.

2.2 Photoionized plasmas: the nebular model

The nebular model (e.g. Kallman & McCray 1982, Liedahl 1999) is intended to describe the physical state and emission of a plasma illuminated by intense X-ray radiation. The most important applications of this model are accretion-powered X-ray sources: active galactic nuclei, X-ray binaries and cataclysmic variables. In these objects, circumsource material is believed to intercept some of the radiation emitted from a compact region near the accreting source and to reprocess it into line and continuum emission in other portions of the spectrum. The main assumption of the nebular model is that the temperature and ionization structure of the illuminated gas are essentially governed by the interactions of the radiation field with the ion-electron plasma. Possible additional heating sources, such as shocks or magnetic-field reconnection, are thus generally neglected.

2.2.1 Ionization structure and thermal equilibrium

The temperature and ionization structure of a photoionized plasma are obviously intimately connected. For example, recombination of thermal electrons affects both the charge state distribution and the plasma cooling rate. Thus, the state of the plasma has to be determined by solving a set of coupled equations describing the ionization balance together with the thermal equilibrium. Most photoionized-plasma models which have been developed so far (see Ferland *et al.* 1995 and references therein) assume that the ionization and energy balances are in a steady-state, i.e. that the time scales for variation in the compact source emission and in the plasma global parameters are long compared to the characteristic time scales for the atomic processes. The ionic fractions of adjacent charge states are then connected through a generalization of eq. (2.3), which obviously has to take into account the dominant process of photoionization, but also the possible contribution of charge-exchange reactions (e.g. Halpern & Grindlay 1980):

$$\eta_Z^i \cdot [\zeta_{Z^{+i}}(F_\epsilon) + n_e C_{Z^{+i}}(T) + K_{Z^{+i}}^I(T)] = \eta_Z^{i+1} \cdot [n_e \alpha_{Z^{+(i+1)}}(T) + K_{Z^{+(i+1)}}^R(T)]. \quad (2.8)$$

Here, $\zeta_{Z^{+i}}(F_\epsilon)$ is the photoionization rate (in units of s^{-1}), which depends on the flux of the illuminating radiation F_ϵ (see below), and $K_{Z^{+i}}^I(T)$ and $K_{Z^{+i}}^R(T)$ are the effective ionization and recombination rates due to charge-transfer reactions (also in s^{-1}), which, for a gas of given composition and density, only depend on the ionic fractions of H and He, and on the plasma temperature T . Ionization by thermal electron impact (of rate coefficient $C_{Z^{+i}}(T)$, § 2.1.1) is often unimportant, because, contrary to coronal plasmas, the temperature of photoionized gas may not reach the ionization threshold energy of many ions. Lower temperatures can also modify the relative contributions of DR and RR to the total recombination rate coefficient $\alpha_{Z^{+(i+1)}}(T)$ (§ 2.1.1): in a photoionized plasma, radiationless dielectronic capture proceeds primarily through core excitations of relatively low energies, i.e. essentially transitions of core electrons to the same shell ($\Delta n=0$ excitations, n being the principal quantum number). Thus, RR generally dominates the total recombination rate for H-like and He-like ions, since these species have no available $\Delta n=0$ excitations. On the other hand, DR can be the main recombination process for ions with partially filled L or M shells (Liedahl 1999 and references therein).

The photoionization rate $\zeta_{Z^{+i}}(F_\epsilon)$ is obtained by folding the radiation field with the corresponding photoionization cross section $\sigma_{Z^{+i}}^{pI}(\epsilon)$:

$$\zeta_{Z^{+i}}(F_\epsilon) = \int_{I_{Z^{+i}}}^{\infty} \frac{F_\epsilon(\epsilon, R)}{\epsilon} \sigma_{Z^{+i}}^{pI}(\epsilon) d\epsilon, \quad (2.9)$$

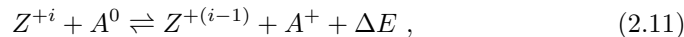
where $I_{Z^{+i}}$ is the ionization threshold energy of ion Z^{+i} and $F_\epsilon(\epsilon, R)$ is the net energy flux at the distance R from the compact source (in c.g.s units of $\text{erg s}^{-1} \text{cm}^{-2} \text{erg}^{-1}$). For example, for an isotropic point source of total luminosity L_ϵ and spectrum $dL_\epsilon/d\epsilon = L_\epsilon s(\epsilon)$, assuming that the source radiation is not significantly

attenuated by photoabsorption, the photoionization rate is simply given by

$$\zeta_{Z+i}(F_\epsilon) = \frac{L_\epsilon}{4\pi R^2} \int_{I_{Z+i}}^{\infty} \frac{s(\epsilon)}{\epsilon} \sigma_{Z+i}^{pI}(\epsilon) d\epsilon . \quad (2.10)$$

However, photoionization is often enhanced by the emission of one or more Auger electrons in addition to the original photoelectron. For example, photoionization of a K-shell electron in an ion having two or more L-shell electrons leaves the resulting ion in an *autoionizing* state that can decay by ejecting at least one L-shell electron. The L-shell vacancy thus produced can further be filled by an other radiationless Auger transition if the ion has two or more M-shell electrons. This cascade process can lead to the ejection of up to eight Auger electrons following the creation of a K-shell vacancy in neutral iron (Kaastra & Mewe 1993). Thus, ionization balance calculations in the framework of the nebular model are generally complicated by the possible coupling of several charge states in each element (Weisheit 1974). Note that additional ionization can be produced by collisions of the fast ejected electrons with neighbouring ions (Halpern & Grindlay 1980). However, if most of ambient H and He are ionized, these electrons will slow down primarily by elastic scattering with thermal electrons, thus depositing their energy as heat.

Charge-transfer reactions can be very important for the ionization structure of a photoionized plasma, if a significant abundance of neutral H or He atoms (i.e. with neutral fraction typically exceeding ~ 0.01) coexists with ionized heavy elements. They are of the form



where $A \equiv \text{H or He}$ and ΔE is the energy defect, which can be either a positive or a negative quantity depending on the reaction and on the atomic states involved in the electron transfer (e.g. Kingdon & Ferland 1999). The rate coefficients are obtained by integrating the reaction cross sections over the Maxwell-Boltzmann distribution of the relative collision velocity. Detailed quantum mechanical calculations were performed for few important reactions. For other systems, the cross sections can be reasonably estimated by use of the Landau-Zener approximation (Kingdon & Ferland 1996 and references therein).

In the nebular model, the plasma temperature is determined by solving the equation of thermal equilibrium:

$$\begin{aligned} n_e \Gamma_e + n_H \sum_Z a_Z \sum_i \eta_Z^i (\Gamma_{Z+i}^{pI} + \Gamma_{Z+i}^{CT}) = \\ n_e \Lambda_{ff} + n_H \sum_Z a_Z \sum_i \eta_Z^i (\Lambda_{Z+i}^R + \Lambda_{Z+i}^C + \Lambda_{Z+i}^{CT}) , \end{aligned} \quad (2.12)$$

where the left- and the right-hand sides represent the total heating and cooling rates ($\text{erg cm}^{-3} \text{ s}^{-1}$) of the thermal bath, respectively. Here, Γ_e is the heat-

ing rate per free electron due to Compton scattering³; $\Gamma_{Z^{+i}}^p$ is the effective photoionization heating rate, which includes heating by the Auger electrons (Shull 1979); $\Gamma_{Z^{+i}}^{CT} = K_{Z^{+i}}^R \text{ or } I \times \Delta E$ is the heating rate due to exothermic ($\Delta E > 0$) charge-transfer recombinations or ionizations (Kingdon & Ferland 1999); Λ_{ff} is the thermal bremsstrahlung cooling rate due to free-free emission (see Marcowith, this volume); $\Lambda_{Z^{+i}}^R$ is the recombination cooling rate due to both RR and DR (Halpern & Grindlay 1980 and references therein); $\Lambda_{Z^{+i}}^C$ is the cooling rate due to collisional excitation or ionization by thermal electron impacts; and $\Lambda_{Z^{+i}}^{CT}$ is the cooling rate due to endothermic ($\Delta E < 0$) charge-transfer reactions. Alternatively, the thermal balance can be established by calculating the rate of removal or addition of energy to the local radiation field associated with each of the processes affecting atomic level populations (Kallman & Bautista 2001).

2.2.2 Line emission

It is instructive to compare the line production in photoionized plasmas and in thermally ionized plasmas. In the coronal model, the electron population responsible for the plasma ionization structure is also an efficient source of collisional line excitation. On the other hand, a photoionized plasma is generally overionized relative to the electron temperature, since the thermal electrons are not the dominant source of ionization. Collisional excitation is then often unimportant in the X-ray energy range and the line emission is preferentially due to recombination of relatively low-energy electrons and to photon-induced fluorescence. Therefore, whereas in the coronal model, line production in ion Z^{+i} is generally proportional to its ionic fraction η_Z^i (eq. 2.6), in the nebular model it is dominated by processes involving adjacent charge states: recombination of ion $Z^{+(i+1)}$ and inner-shell photoionization of ion $Z^{+(i-1)}$. This difference allows to distinguish between coronal and nebular gas emission of cosmic origin by observing various line intensity ratios from the same element. For example, Liedahl *et al.* (1990) have shown that the $(3s \rightarrow 2p)/(3d \rightarrow 2p)$ line ratios from Fe XVII-XIX can be used to discriminate between thermally ionized and photoionized plasmas, because the $3d$ lines are preferentially produced by electron impact excitation in a hot coronal plasma (5-10 MK, see Fig. 2), whereas the $3s$ lines are mostly formed by recombination in a cooler (~ 0.1 MK) nebular plasma.

Line emission in the X-ray energy range is dominated by the K lines of C, N, O,

³ Compton scattering is generally the dominant heating process of X-ray-emitting photoionized plasmas. The net rate coefficient expressing the excess of Compton heating over Compton cooling can be written as (Ross 1979):

$$\Gamma_e = \frac{\sigma_T}{m_e c^2} \left[\int_0^\infty \left(\epsilon - \frac{21}{5} \frac{\epsilon^2}{m_e c^2} \right) F_\epsilon(\epsilon, R) d\epsilon - 4kT \int_0^\infty F_\epsilon(\epsilon, R) d\epsilon \right], \quad (2.13)$$

where σ_T is the Thomson cross section and c is the speed of light. The first term in the brackets represents the heating of relatively cold electrons by scattering with X-rays and includes the first order Klein-Nishina correction, and the second term represents the cooling of hot electrons by scattering with lower energy photons (see also Marcowith, this volume).

Ne, Mg, Si, Ar, Ca, Fe and Ni and the L lines of Fe and Ni. Thus, recombination lines are produced in relatively highly ionized ions, having in their ground state at least one K-shell vacancy, or one L-shell vacancy for Fe^{+i} and Ni^{+i} . On the other hand, fluorescent lines being due to radiative transitions from the L or M shell following inner-shell photoionization, they are generally associated with colder, less ionized plasmas.

Recombination radiation in overionized plasmas has been observed from several high mass X-ray binaries (e.g. Sako *et al.* 1999 and references therein). It consists of radiative recombination ‘‘continua’’ (see below) and lines produced through recombination to excited states followed by radiative cascades. The volume emissivity (photons $\text{cm}^{-3} \text{s}^{-1}$) of a given line transition $a \rightarrow b$ in ion Z^{+i} can be written as

$$P_{Z^{+i}}^{ab} = n_e n_H a_Z \eta_Z^{i+1} \alpha_{Z^{+(i+1)}}^a B_{ab}, \quad (2.14)$$

where $\alpha_{Z^{+(i+1)}}^a$ is the effective recombination rate coefficient to the level a (including recombination to higher levels followed by radiative transitions to level a) and the other quantities are defined above in eq. (2.6). Radiative recombination continuum (RRC) is produced by the first free-bound transition. The monochromatic specific emissivity (photons $\text{s}^{-1} \text{cm}^{-3} \text{erg}^{-1}$) from radiative capture of a free electron of velocity v is given by

$$\frac{dP_{Z^{+i}}^{RRC}}{d\epsilon}(\epsilon) = n_e n_H a_Z \eta_Z^{i+1} v f(v) \sigma_{Z^{+(i+1)}}^{RR}(v) \frac{dv}{d\epsilon}, \quad (2.15)$$

where the energy of the radiated photon is equal to the sum of the ionization potential of the recombined ion $(Z^{+i})^*$, which may or may not be formed in an excited state, plus the kinetic energy of the recombining electron,

$$\epsilon = I_{(Z^{+i})^*} + \frac{1}{2} m_e v^2, \quad (2.16)$$

$f(v)$ is the thermal electron velocity distribution (eq. 2.5) and $\sigma_{Z^{+(i+1)}}^{RR}(v)$ is the radiative recombination cross section, which is related to the corresponding photoionization cross section through the Milne equation (see e.g. Mewe 1999):

$$\sigma_{Z^{+(i+1)}}^{RR}(v) = \frac{g_{(Z^{+i})^*}}{g_{Z^{+(i+1)}}} \cdot \frac{\epsilon^2}{(m_e v c)^2} \cdot \sigma_{(Z^{+i})^*}^{pI}(\epsilon). \quad (2.17)$$

Here, $g_{Z^{+i}} = 2J_{Z^{+i}} + 1$ is the statistical weight of ion Z^{+i} , whose total angular momentum is $J_{Z^{+i}}$. Combining these equations provides the RRC emissivity as a function of the electron temperature:

$$\frac{dP_{Z^{+i}}^{RRC}}{d\epsilon}(\epsilon) = \sqrt{\frac{2}{\pi}} \cdot \frac{g_{(Z^{+i})^*}}{g_{Z^{+(i+1)}}} \cdot \frac{n_e n_H a_Z \eta_Z^{i+1} c \sigma_{(Z^{+i})^*}^{pI}(\epsilon) \epsilon^2}{(m_e c^2 k T_e)^{3/2}} \cdot \exp \left[- \frac{(\epsilon - I_{(Z^{+i})^*})}{k T_e} \right]. \quad (2.18)$$

The photoionization cross sections are rapidly decreasing functions of photon energy from ionization thresholds. For example, they are about proportional to ϵ^{-3}

for hydrogenic ions (see also Fig. 6a). We see from the above equation that the RRC emissivities are steep functions of energy as well. In photoionized plasmas, the RRC emissions often appear as relatively narrow features in the spectrum (sometimes “line-like” features), with approximate width $\Delta\epsilon \sim kT_e$ (Liedahl 1999). Analyses of RRC shapes can thus allow determination of the electron temperature of the emitting plasma.

Fluorescent line emission has been observed from a number of Galactic X-ray binaries (e.g. Ebisawa *et al.* 1996, Sako *et al.* 1999) and active galactic nuclei (Fabian *et al.* 2000 and references therein). It is produced when an inner-shell photoionization is followed by a radiative transition. The volume emissivity of a fluorescent line $a \rightarrow b$ is thus given by

$$P_{Z^{+(i+j)}}^{ab} = n_H a_Z \eta_Z^{i-1} \zeta_{Z^{+(i-1)}}^{a'} (F_\epsilon) \omega_{Z^{+i}}^{ab}, \quad (2.19)$$

where $\zeta_{Z^{+(i-1)}}^{a'}(F_\epsilon)$ is the inner-shell photoionization rate of ion $Z^{+(i-1)}$, leading to ion Z^{+i} in the excited level a' (see eqs. 2.9 and 2.10) and $\omega_{Z^{+i}}^{ab}$ is the $a \rightarrow b$ line fluorescence yield, i.e. the number of photons emitted in the line $a \rightarrow b$ per ion Z^{+i} in the level a' . Note that the line $a \rightarrow b$ is not necessarily produced in ion Z^{+i} , since the first decay of the level a' can be an Auger transition to an excited state a'' of ion $Z^{+(i+1)}$. Auger electron emission can repeat several times before the line $a \rightarrow b$ is emitted in ion $Z^{+(i+j)}$ and the calculation of the overall process can become cumbersome, since millions of transitions can follow a single inner-shell ionization. For example, 5.1 millions of Auger or radiative transitions are possible after an Fe I K-shell ionization (Kaastra & Mewe 1993). The convention is therefore to refer to the inner-shell vacancy produced in ion $Z^{+(i-1)}$, rather than to the excited atomic level a' of ion Z^{+i} . For example, we speak of the $K\alpha$ fluorescence yield for *neutral* Fe (for which I will adopt the notation $\omega_{Fe}^{K\alpha} \equiv \omega_{Fe^{+0}}^{K\alpha}$), although this quantity strictly describes an atomic property of ion Fe^{+1} .

The fluorescence yield is a strongly increasing function of ion atomic number z . For example, $\omega_Z^K = \omega_Z^{K\alpha} + \omega_Z^{K\beta}$ varies approximately as $z^{3.25}$ for a K-shell vacancy produced in neutral atoms up to Fe (Krause 1979). That explains why the most prominent fluorescent line observed so far is the $K\alpha$ line from weakly-ionized Fe, since this element has the highest product of $K\alpha$ fluorescence yield ($\omega_{Fe^{+i}}^{K\alpha} = 0.305 \pm 0.001$ for Fe I-IX, Kaastra & Mewe 1993) and cosmic (i.e. solar) abundance ($a_{Fe} = 3.2 \times 10^{-5}$, Anders & Grevesse 1989). The line emission at ~ 6.4 keV is often accompanied by a sharp absorption edge at 7.1 keV, the K-shell electron binding energy in neutral or weakly-ionized Fe: nearly 30% ($= \omega_{Fe^{+i}}^{K\alpha}$) of the photons absorbed above this threshold energy are “re-emitted” in the Fe $K\alpha$ line.

However, if the nebular plasma is optically thick to the ionizing continuum in some portions of the spectrum, radiative transfer is generally important and has to be taken into account from a geometrical model of the emitting source (e.g. Fabian *et al.* 2000). The problem of continuum and line transfer at intermediate optical depth is a difficult one and is generally tackled from approximate solutions to the full transfer equation (e.g. Kallman & Bautista 2001). It is particularly

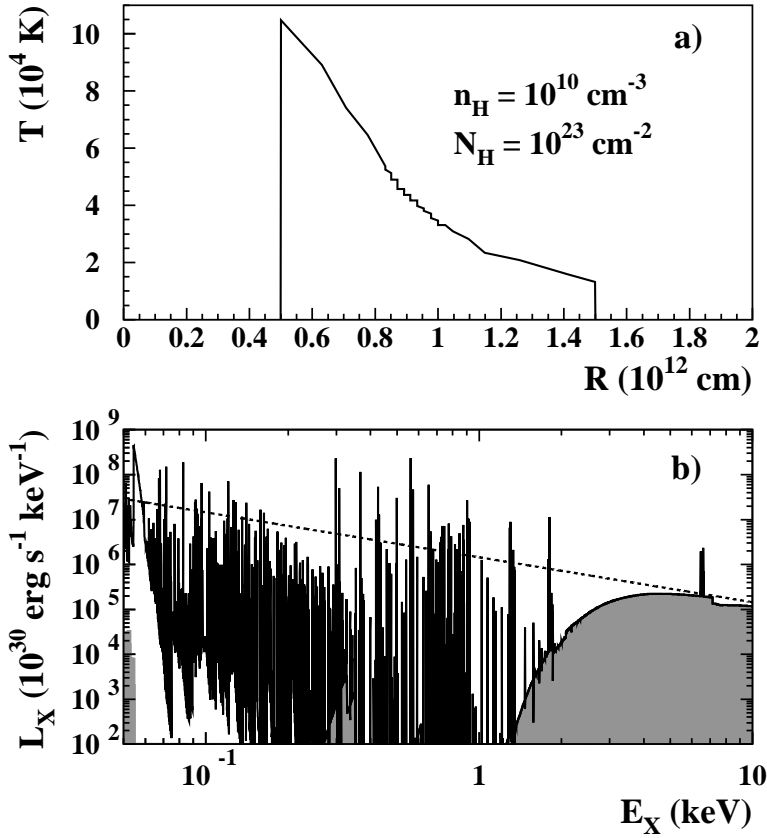


Fig. 4. Calculated thermal structure (a) and emission (b) of a spherical gas shell of solar composition and constant H density (irrespective of its charge state), $n_H=10^{10}$ cm $^{-3}$, illuminated by a steady state, isotropic point source at $R=0$. In panel (b), the dashed line is the source spectrum, $L_X^{in}(E_X)=1.45\cdot 10^{36}\times E_X^{-1}$ erg s $^{-1}$ keV $^{-1}$, and the grey area shows the source emission after transmittance through the shell. The total emerging spectrum (solid line) is the sum of the transmitted source emission plus the thermal radiation (mostly recombination radiation) and fluorescence emission from the photoionized shell.

relevant for resonance lines, which correspond to allowed transitions to ground ionic levels and can be emitted following radiative recombination or collisional excitation. Indeed, photons emitted in such lines can have a high probability to be absorbed by the same transition which emitted them and “re-emitted” at a new frequency. This frequency redistribution can repeat many times until the photon either escapes the gas or is destroyed by photoabsorption (e.g. Faurobert 1986).

By way of illustrated summary, I show in Figure 4 calculated thermal structure and emission of a spherical gas shell photoionized by a central source. I used

the XSTAR version 2.1h computer code developed by Kallman *et al.*⁴. We see in panel (a) that the temperature is found to decrease from $\sim 10^5$ K ($kT \sim 8.6$ eV) in the internal region of the shell to nearly 10^4 K in the outermost region. Thus, collisional excitation is negligible in the X-ray energy range and the line emission in panel (b) is mostly due to radiative recombination. The Fe $K\alpha$ fluorescent line emission at ~ 6.5 keV and the corresponding absorption above 7.1 keV are also visible. The irregular continuum emission from the photoionized shell is produced by overlapping radiative recombination continua and two-photon decays of metastable levels, which cannot decay by a single-photon transition⁵ (thermal bremsstrahlung is negligible in this energy domain). The most prominent RRC in panel (b) is the triangular feature just above 54 eV (i.e. in the extreme ultraviolet waveband), produced by free electron recombination to the K-shell of fully-ionized He.

2.3 Plasma diagnostics from X-ray line emission

As already mentioned, simple spectroscopic analyses of the X-ray line emission from a hot plasma can provide valuable information, such as the ionization processes (photoionization and/or collisional ionization), the elemental abundances and the ionization balance. The recent launch of X-ray instruments with high sensitivity and spectral resolution, such as the grating spectrometers aboard the *XMM-Newton* and *Chandra* satellites, allows more refined diagnostics of plasma parameters, among which those based on satellite lines and helium-like line triplets may deserve special attention.

Satellite lines are produced by stabilizing transitions in the process of dielectronic recombination (§ 2.1.1). The most important of such lines arise from the dielectronic capture of a free electron into the L-shell and appear on the long-wavelength side of the parent resonance line. For example, the relatively strong satellite line $j \equiv 1s2p^2[{}^2D_{5/2}] \rightarrow 1s^22p[{}^2P_{3/2}]$ is at 6.744 \AA (1.838 keV) for Li-like Si XII, whereas the corresponding resonance line $w \equiv 1s2p[{}^1P_1] \rightarrow 1s^2[{}^1S_0]$ in He-like Si XIII is at 6.647 \AA (1.865 keV; Gabriel 1972). The DR satellite-to-resonance line intensity ratios are very sensitive to the electron temperature of a coronal

⁴ See <http://heasarc.gsfc.nasa.gov/docs/software/xstar/xstar.html> .

⁵ The simultaneous emission of two photons is important for H- and He-like ions in the excited states $n^{2S+1}L_J \equiv 2^2S_{1/2}$ and 2^1S_0 , respectively. In this usual notation, n is the principal quantum number of the outermost occupied shell; L is the total orbital quantum number, which, in the Russell-Saunders LS -coupling, is given by the vectorial sum of the individual electron orbital angular momenta; S is the total spin angular momentum, obtained by the vectorial coupling of the spin angular momentum ($s=1/2$) of all the electrons ($r=2S+1$ is called the multiplicity of the level); and J is the total angular momentum, which is the vector sum $L+S$ for LS coupling. The orbital quantum number L is usually designated by the symbols S, P, D, F, G, \dots (corresponding to “sharp”, “principal”, “diffuse”, “fundamental” and the subsequent letters to the alphabetical order) for $L=0,1,2,3,4, \dots$. Thus, the level $2^2S_{1/2}$ of H-like ions corresponds to the electron being in the $2s$ subshell and the level 2^1S_0 of He-like ions to the two electrons being in the $1s$ and $2s$ subshells with antiparallel spins ($S=0$). It follows from the quantum selection rules that for these two levels, the $2s$ electron cannot decay by a single-photon transition (e.g. Sobelman 1979).

plasma. This is fundamentally due to the resonant character of the DR process (Fig. 1) compared to the collisional excitation process: a DR satellite line is produced only by free electrons of energy close to the excitation energy of the satellite line level (within the small level width), whereas a resonance line can be excited by all electrons with any energy above the resonance line energy. This also provides a way to evaluate a possible deviation of the electron velocity distribution from a Maxwellian distribution. Thus, the existence of a high-energy tail of nonthermal electrons in turbulent plasmas could be identified through an increase of the resonance line intensities relative to the DR satellite line intensities (Gabriel & Phillips 1979).

Collisional inner-shell excitation (IE) can also contribute to the emission of certain satellite lines, such as the line $q \equiv 1s2s2p[{}^2P_{3/2}] \rightarrow 1s^22s[{}^2S_{1/2}]$ (at 6.718 Å in Si XII). Because the simultaneous excitation of two electrons is generally highly improbable, some lines (j for example) can only be produced from excited state configurations ($1s^22p$ for line j), which are negligible in low-density plasmas. However, these excited levels can obtain a significant population at equilibrium for high electron density (e.g. at $n_e \sim 10^{17} \text{cm}^{-3}$ for Si XII), thus introducing a density dependence of satellite lines.

The intensity ratio of a IE satellite line to its parent resonance line is almost independent of temperature, since these two lines are excited by nearly the same electron population. However, it does depend on the plasma ionization structure, as the intensity of an IE satellite line in ion Z^{+i} is proportional to the ionic fraction η_Z^i , whereas the intensity of the corresponding resonance line in ion $Z^{+(i+1)}$ is proportional to η_Z^{i+1} . Thus, satellite lines can also provide diagnostics of the ionization state of a transient plasma.

I now briefly present diagnostics based on the well-known He-like $n=2 \rightarrow 1$ line triplet. This system consists of three close lines (Fig. 5): the resonance $E1$ line w , the forbidden magnetic dipole ($M1$) line z and the intercombination line $x+y$, which is made of two unresolvable components that violate the selection rule $\Delta S=0$ (see footnote 2) because of magnetic interactions. In Si XIII for example, the lines are at 6.684 Å, 6.687 Å and 6.739 Å, for the x , y and z transitions, respectively. As first shown by Gabriel & Jordan (1969), the emissivity ratio of the forbidden to intercombination lines,

$$R_{Z^{+i}} = \frac{P_{Z^{+i}}^z}{P_{Z^{+i}}^x + P_{Z^{+i}}^y}, \quad (2.20)$$

is strongly sensitive to the electron density above a certain value ($\sim 5 \cdot 10^{12} \text{cm}^{-3}$ for Si XIII and $\sim 5 \cdot 10^7 \text{cm}^{-3}$ for C V). This is due to the collisional excitation of the metastable level 2^3S_1 to the close levels $2^3P_{0,1,2}$, which leads to a decrease of the $R_{Z^{+i}}$ ratio with increasing electron density. This density measurement can be applied to recombination dominated plasmas as well as to coronal plasmas. However, photoexcitation of the 2^3S_1 level to the 2^3P term may not be negligible for photoionized plasmas illuminated by intense ultraviolet radiation (Porquet *et al.* 2001b and references therein).

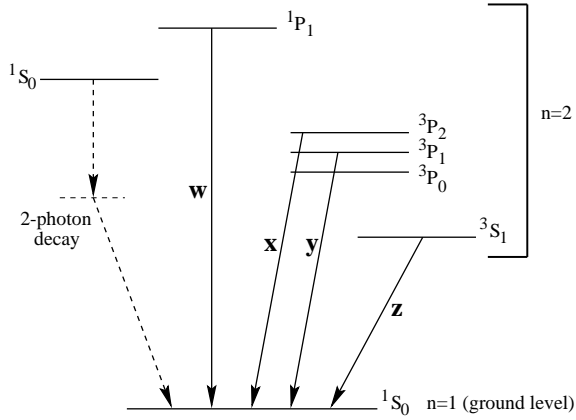


Fig. 5. Scheme of the first energy levels of He-like ions (simplified Gotrian diagram). The He-like triplet is formed by the resonance line w , the intercombination line $x+y$ and the forbidden line z . Also shown is the continuum-producing, two-photon decay of the level 2^1S_0 .

Gabriel & Jordan (1969) also showed that the emissivity ratio

$$G_{Z+i} = \frac{P_{Z+i}^z + (P_{Z+i}^x + P_{Z+i}^y)}{P_{Z+i}^w} \quad (2.21)$$

can be used to diagnose the electron temperature of a coronal plasma, since the collisional excitation rates have not the same temperature dependence for the resonance line as for the forbidden and intercombination lines. This ratio can also serve as an indication of the validity of the coronal model (e.g. Porquet & Dubau 2000). Indeed, a strong resonance line is expected in plasmas dominated by collisional excitation. On the other hand, since radiative recombinations to the 2^3S and 2^3P triplet terms are favored as compared with the 2^3P_1 level, a significant contribution of photoionization leads to a relatively high G_{Z+i} ratio (see also Liedahl 1999). Porquet & Dubau (2000) and Porquet *et al.* (2001b) have recently provided detailed calculations of the line ratios R_{Z+i} and G_{Z+i} for the most important He-like ions.

Satellite lines and He-like triplet lines have proven to be very useful to characterize laboratory plasmas, as well as coronal plasmas heated by solar flares (e.g. Harra-Murnion *et al.* 1996). The new generation of X-ray spectrometers now allows to use the same powerful diagnostics for cosmic sources (e.g. Weisskopf *et al.* 2002 and references therein; see also Ballet, this volume).

3 Nonthermal X-ray line production from accelerated particle interactions

Nonthermal electron and ion populations are expected to occur in various astrophysical plasmas, when kinetic energy is deposited by acceleration processes into the tail of the distributions, at a rate that is sufficiently high to overcome the thermal equilibration processes. The impacts of a nonthermal electron tail on the ionization balance and X-ray line emission of such “hybrid” plasmas were first studied for solar flares and more recently for supernova remnants and clusters of galaxies (e.g. Porquet *et al.* 2001a and references therein). In the following, I consider nonthermal X-ray line production in a different context, namely from nonthermal particles escaping from the acceleration region and interacting in a distinct target medium. It is the most usual situation in laboratory experiments, but paradoxically, it has received little attention in astrophysics.

3.1 Accelerated electron interactions

Fast electrons interacting in an ambient medium can produce X-ray lines by collisional excitation and inner-shell ionization. Nonthermal X-ray line production by suprathermal electron interactions has been proposed to account for the observation in impulsive solar flares of enhanced Fe K α line emission at ~ 6.4 keV that is coincident with the hard X-ray burst (Zarro *et al.* 1992). Recently, Valinia *et al.* (2000) suggested that the interaction of low-energy cosmic-ray electrons with interstellar matter could make a significant contribution to the Fe K line complex observed in the spectrum of the Galactic ridge X-ray background.

Here, I assume for simplicity that the interaction region is composed of neutral atoms, such that X-ray line emission can result from inner-shell ionization but not from collisional excitation. However, the fast electrons can also produce continuum hard X-rays via nonthermal bremsstrahlung, which in turn can produce fluorescent line emission via photoionization. Thus, each line can generally result from a combination of collisional ionization and photoionization, with relative contributions depending on the accelerated electron spectrum and on ambient medium parameters. I now discuss some fundamental differences between the two atomic processes.

A compilation of cross sections for K-shell ionization is shown in Figure 6a. We see that whereas the photoionization cross sections are steep functions of energy (they vary approximately as E_X^{-3} from ionization thresholds) the cross sections for collisional ionization have a much harder energy dependence, in particular, a rise in the MeV region caused by relativistic effects (e.g. Hoffmann *et al.* 1979). Thus, while fluorescence is essentially produced by photons with energy contained in a range of a few keV above the ionization threshold, ultra-relativistic electrons can still produce significant X-ray line emission. We also see that the relative contributions of collisional ionization and photoionization will generally depend on the target element Z . Numerically, the K-shell ionization cross section scales approximately as $z^{-4.3}$ for the electrons, whereas it scales about as $z^{-2.3}$ for the

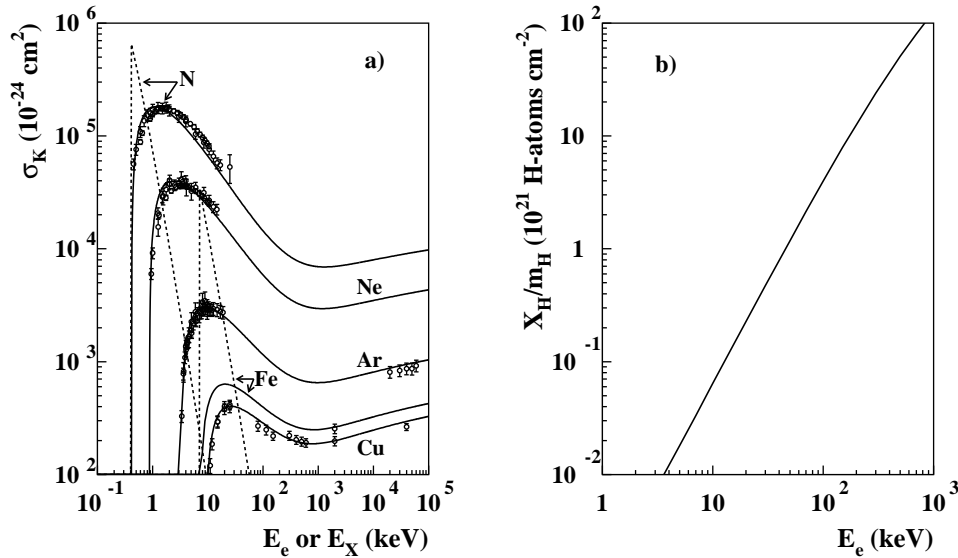


Fig. 6. (a) Solid curves and data points: cross sections for K-shell ionization of various atoms by electron impact. Cross sections calculated from the semi-empirical formula of Quarles (1976) are compared with data compiled in Long *et al.* (1990). Dashed curves: cross sections for K-shell photoionization of N and Fe (Verner *et al.* 1993). (b) Stopping range of low-energy electrons in hydrogen. The plotted quantity is X_H/m_H , where X_H is the stopping range in c.g.s. units of g cm^{-2} from Berger & Seltzer (1982) and m_H is the mass of the H-atom.

photons.

Propagation makes an other important difference between electron- and photon-induced ionization. Figure 6b shows the stopping range of low-energy electrons in a neutral H gas. Taking into account ambient He with $(n_{He}/n_H)=0.1$ reduces the plotted range, measured in H-atoms cm^{-2} , by a factor of ~ 1.18 . Thus, suprathermal electrons < 100 keV injected in a neutral atomic gas of solar composition would stop in 4×10^{21} H-atoms cm^{-2} . As we will see below, these electrons could produce in such a thick target an observable Fe $K\alpha$ line emission. In comparison, the optical depth of > 7.1 keV X-rays with respect to photoelectric absorption is $\tau_{abs} < 0.01$ for $N_H = 4 \times 10^{21} \text{ cm}^{-2}$, such that Fe K-shell ionizing photons would barely interact in the target region.

As a basic introduction to nonthermal processes, let us now calculate the X-ray emission produced by the interaction of a steady state, suprathermal electron source with a thick target composed of neutral atoms with solar abundances. For simplicity, I assume that the nonthermal electron population does not modify the state of the ambient medium, i.e. that ionization and heat deposition are negligible. I further assume that the typical column density of the interaction region is sufficiently low to safely neglect the fluorescent line emission due to photoioniza-

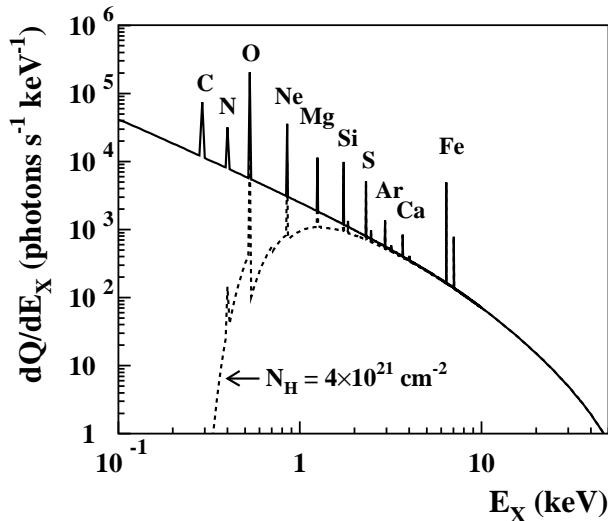


Fig. 7. X-ray emission produced by suprathermal electrons with the source spectrum of eq. (3.4) interacting in a thick target composed of a neutral atomic gas of solar abundance. The X-ray lines are plotted as delta functions in energy bins of 10 eV. The dashed line shows the effect of photoelectric absorption, with a H column density of $4 \times 10^{21} \text{ cm}^{-2}$ (see text).

tion of the ambient atoms by the bremsstrahlung X-rays. The differential X-ray production rate (photons $\text{s}^{-1} \text{ keV}^{-1}$) can then be written as

$$\frac{dQ}{dE_X}(E_X) = \int_0^\infty \frac{dN_e}{dt}(E_e) \times \left[n_H \sum_Z a_Z \int_0^{E_e} \frac{d\sigma_Z}{dE_X}(E_X, E') \frac{dE'_e}{(dE/dl)(E'_e)} \right] dE_e, \quad (3.1)$$

where (dN_e/dt) is the differential injection rate of suprathermal electrons into the target region, measured in electrons $\text{s}^{-1} \text{ keV}^{-1}$, $(d\sigma_Z/dE_X)$ is the differential X-ray production cross section for electron interactions with atoms Z ($\equiv Z^{+0}$) and (dE/dl) is the electron energy loss rate per unit path length in the ambient medium, measured in keV cm^{-1} . In this equation, the term in the brackets gives the monochromatic X-ray production by an electron of energy E_e as it slows down to rest in the ambient medium, which has to be integrated over the energy distribution of the nonthermal electrons.

As H and He are by far the most abundant constituents of the interaction region, we have

$$\left(\frac{dE}{dl} \right) \cong n_H \left[m_H \left(\frac{dE}{dx} \right)_H + a_{He} m_{He} \left(\frac{dE}{dx} \right)_{He} \right], \quad (3.2)$$

where m_H and m_{He} are the H- and He-atom masses, and $(dE/dx)_H$ and $(dE/dx)_{He}$ are the electron stopping powers (in units of $\text{keV g}^{-1} \text{ cm}^2$) in ambient H and He,

respectively (Berger & Seltzer 1982). Inserting eq. (3.2) into eq. (3.1), we see that under the assumption of thick target interactions, the X-ray production rate depends on the relative abundances a_Z of the ambient medium constituents, but *not on the density*.

I consider for the X-ray line production the $K\alpha$ and $K\beta$ ($3p \rightarrow 1s$) lines from ambient C, N, O, Ne, Mg, Si, S, Ar, Ca and Fe. The corresponding cross sections can be written as

$$\frac{d\sigma_Z^{Ki}}{dE_X}(E_X, E_e) = \delta(E_X - E_{Ki})\sigma_Z^I(E_e)\omega_Z^{Ki}, \quad (3.3)$$

where E_{Ki} is the energy of line Ki ($K\alpha$ or $K\beta$), $\delta(E_X - E_{Ki})$ is Dirac's delta function, $\sigma_Z^I(E_e)$ is the cross section for the K-shell ionization of atom Z by an electron of energy E_e (Quarles 1976) and ω_Z^{Ki} is the Ki fluorescence yield for atom Z (Firestone 1996, appendix F, and references therein). Note that $\omega_Z^{K\beta} = 0$ for $z \leq 12$ (i.e. Mg), since these atoms do not have $3p$ electrons in their ground level. For the X-ray continuum emission, I take into account electron bremsstrahlung in ambient H and He only and calculate the corresponding differential cross sections from equation (3BN) in Koch & Motz (1959), with the Elwert correction factor which is appropriate at nonrelativistic energies.

The result is shown in Figure 7 (solid line) for the differential injection rate of suprathermal electrons

$$\begin{aligned} \frac{dN_e}{dt}(E_e) &= 2.71 \cdot 10^8 \times E_e^{-2} \text{ electrons s}^{-1} \text{ keV}^{-1}, \text{ for } 10 < E_e < 100 \text{ keV}; \\ \frac{dN_e}{dt}(E_e) &= 0, \text{ for } E_e < 10 \text{ keV or } E_e > 100 \text{ keV}. \end{aligned} \quad (3.4)$$

However, the calculated emission is obviously not realistic, since the assumption that the target region is sufficiently thick to stop < 100 keV electrons implies that some photoelectric absorption must occur. It generally has to be taken into account from a geometrical model of the emitting region. In Figure 7, the dashed line spectrum is intended for providing a simple illustration of the effect of photoelectric absorption. It is obtained by multiplying (dQ/dE_X) by $\exp(-N_H\sigma_{abs}(E_X))$, where $\sigma_{abs}(E_X)$ is the absorption cross section per H-atom of a medium of cosmic composition (Morrison & McCammon 1983) and N_H is the mean H column density from the site of X-ray production to the edge of the emitting region. I adopted for this quantity the stopping range of 100 keV electrons in the ambient medium, $N_H = 4 \times 10^{21} \text{ cm}^{-2}$.

The normalization of the source spectrum has been chosen such that the power continuously deposited by the electrons in the interaction region is

$$\dot{W} = \int_0^\infty E_e \frac{dN_e}{dt}(E_e) dE_e = 1 \text{ erg s}^{-1}. \quad (3.5)$$

In comparison, the total luminosity of the X-ray emission is

$$L_X < \int_{0.1 \text{ keV}}^{100 \text{ keV}} E_X \frac{dQ}{dE_X}(E_X) dE_X = 4.2 \times 10^{-5} \text{ erg s}^{-1}. \quad (3.6)$$

This low radiation yield, $R_X=L_X/\dot{W}$, illustrates that X-ray production by suprathermal electrons should generally not be efficient: in a neutral target region, almost all of the electron kinetic energy is preferentially used to ionize ambient H and He, whereas if these two species are already ionized, the fast electrons will lose most of their energy by collective long-range Coulomb interactions.

However, the main conclusion of this exercise is that nonthermal bremsstrahlung should often be accompanied by observable X-ray lines below 10 keV. In Figure 7, the $K\alpha$ lines from O, Ne, Si and Fe are the four most intense, with calculated equivalent widths of 355, 107, 73 and 290 eV, respectively⁶. A significant line emission from elements of relatively low atomic number, such as O and Ne, could allow to distinguish X-ray line production by suprathermal electrons from fluorescence emission. This is because in the case of electron impact, the strong decrease of the fluorescence yields with decreasing atomic number z is compensated by the approximate $z^{-4.3}$ dependence of the K-shell ionization cross section (Fig. 6a).

3.2 Accelerated ion interactions

Low-energy accelerated ions can produce X-rays by a variety of atomic processes (Tatischeff *et al.* 1998 and references therein; Dogiel *et al.* 1998). A calculated nonthermal X-ray spectrum from accelerated ion interactions is shown in Figure 8. As for the suprathermal electrons, I have considered a steady state, thick target interaction model, in which accelerated ions are injected at a constant rate into a neutral ambient medium of solar composition and produce X-rays as they slow down to energies below the thresholds of the various reactions. The differential X-ray production rate is calculated from an equation similar to eq. (3.1), but containing two more summations: one over the elemental abundances of the fast ions and the other one over their ionization states. I assumed that the energetic particles have the same composition as the Galactic cosmic-ray ions at their acceleration sources (see Ramaty *et al.* 1996, table 1). Their ionic fractions are calculated under the assumption that the steady-state nonthermal ion population is at the ionization equilibrium in the interaction region (see eq. 2.3 and Tatischeff *et al.* 1998). I employed the same source spectrum for all ion species,

$$\frac{dN_i}{dt}(E_i) \propto E_i^{-1.5} e^{-E_i/E_0} , \quad (3.7)$$

which could result from strong shock acceleration in the nonrelativistic energy domain (Ramaty *et al.* 1996). Here, E_i is the kinetic energy of the fast ions, measured in MeV nucleon⁻¹, and E_0 is a parameter introduced by Ellison & Ramaty (1985) for solar flare acceleration, which is related to the shock size and the acceleration time. For both clarity and simplicity, photoelectric absorption in the ambient medium is not taken into account.

⁶ The equivalent width is the ratio of the line intensity to the intensity per unit energy interval of the underlying continuum at the line energy.

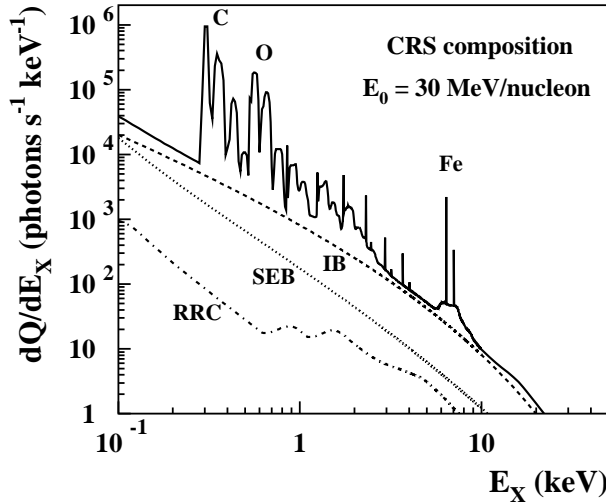


Fig. 8. X-ray emission produced by fast ions with cosmic-ray source (CRS) composition and the source spectrum of eq. (3.7) with $E_0=30$ MeV/nucleon. The calculation is normalized to a power of 1 erg s^{-1} deposited by the accelerated particles in the interaction region. The total luminosity of the calculated X-ray emission (see eq. 3.6) is $4.8 \times 10^{-5} \text{ erg s}^{-1}$. Note that photoelectric absorption in the ambient medium is not taken into account, such that this value is to be considered as an upper limit. IB: inverse bremsstrahlung; SEB: secondary electron bremsstrahlung; RRC: radiative recombination continuum.

Continuum X-rays are essentially produced by inverse bremsstrahlung (IB), which is the kinematic inverse of normal bremsstrahlung, i.e. the radiation of an electron at rest in the moving Coulomb field of a fast ion. Thus, for non-relativistic protons of kinetic energy E_p interacting in stationary H, the inverse bremsstrahlung cross section is almost identical to the bremsstrahlung cross section for electrons of energy $(m_e/m_p)E_p$ also interacting in stationary H⁷. Also shown in Figure 8 are the two continuum emissions from the radiative recombinations of ambient electrons to the K-shell of the fast ions (RRC; Dogiel *et al.* 1998, Tatischeff & Ramaty 1999) and from the secondary, knock-on electrons that subsequently produce bremsstrahlung by interacting with the ambient atoms (SEB). These two emissions should generally be dominated by the IB production.

The narrow lines are due to K-shell vacancy production in the ambient atoms by the fast ions. In comparison with the similar lines produced by electron impact or by photoionization, the lines produced by heavy ion collisions could be shifted

⁷ Baring *et al.* (2000) have recently shown that in shocked astrophysical plasmas, IB from accelerated ions is generally expected to be much lower than bremsstrahlung from suprathermal electrons.

by several tens of electron-volts, significantly broadened and split up into several components, owing to multiple simultaneous ionizations (Garcia *et al.* 1973)⁸. For example, the neutral Fe $K\alpha$ line produced by 1.9 MeV/nucleon O impacts is blueshifted by ~ 50 eV in comparison with that produced by proton impacts, and has a full width at half-maximum (FWHM) of ~ 100 eV (see figure 3.55 of Garcia *et al.* 1973). Such spectral signatures are within the capabilities of modern X-ray instruments.

The prominent, broad line features in Figure 8 are due to atomic de-excitations in the fast ions following electron capture by charge-transfer reactions and collisional excitation. We have considered the $K\alpha$ and $K\beta$ lines from H- and He-like C, N, O, Ne, Mg, Si, S and Fe (Tatischeff *et al.* 1998). These lines should generally be broad for a steady-state nonthermal population at ionization equilibrium, because they are produced by de-excitations of fast moving ions⁹. For example, the O lines in Figure 8 are produced at ~ 1 MeV/nucleon. The Fe broad lines are emitted at ~ 10 MeV/nucleon and merge together to produce a characteristic bump in the spectrum, of width $\cong 2$ keV. However, if the ambient medium is partially ionized, since charge exchange could then be considerably reduced, the fast ions can significantly slow down before capturing electrons, thus producing narrower lines.

Similar line emission has recently been observed from comets, most probably as a result of charge exchange between solar wind particles and cometary neutral gazes (e.g. Lisse *et al.* 2001). However, the observed lines are much narrower than those of Figure 8, because the solar wind ions remain in high charge states at low energies (about 1 keV/nucleon), since they do not reach the ionization equilibrium in the interplanetary space. There are as yet no astrophysical observations from sources outside of the solar system that would unambiguously indicate an origin resulting from relatively low-energy, accelerated ion interactions. Together with nonthermal gamma-ray line production (§ 4.2), X-ray line emission from charge exchange may probably be one of the most promising signatures of such interactions and could provide, in particular, one of the best ways of studying Galactic cosmic-ray ions at energies below 100 MeV/nucleon.

4 Gamma-ray line production from nuclear collisions

Let's now zoom in on the atomic nucleus, from the Angström atomic scale to the Fermi nuclear scale. Nuclear collisions can lead to gamma-ray line emission in a variety of ways. These include the direct excitation of nuclear levels, the production of excited secondary nuclei, the production of radioactive species decaying into excited states of daughter isotopes and the production of neutrons and positrons. The latter can originate from the decay of both β^+ -emitting radionuclei and π^+

⁸ These effects are not taken into account in the present calculations. In Figure 8, the narrow lines are simply plotted as delta functions in energy bins of 10 eV.

⁹ The present calculations assume isotropic interactions, leading to the maximum possible Doppler broadening.

mesons, as well as from the de-excitation of nuclear levels by e^+e^- pair emission (Kozlovsky *et al.* 1987). Positron annihilation and the accompanying processes of positronium formation and annihilation are fundamentally important in almost all of high-energy astrophysics, as first pointed out by Stecker (1969). It is considered in § 6. In the present section, I first discuss the gamma-ray line emission from thermonuclear reactions in high-temperature plasmas (§ 4.1), then consider the nonthermal gamma-ray line production from accelerated ion interactions (§ 4.2) and finally treat the line emission at 2.22 MeV resulting from the radiative capture of free neutrons by ambient protons (§ 4.3).

4.1 Thermonuclear gamma-ray line production

Thermonuclear reactions are responsible for the nucleosynthesis of the elements in stars, but the associated gamma-ray production can not be observed because stars are opaque to gamma-rays. Observable thermonuclear gamma-ray line emission must be produced in optically thin astrophysical plasmas with ion temperature $T_i \gtrsim 10^9$ K ($kT_i \gtrsim 0.086$ MeV). Such high-temperature plasmas are believed to exist in the vicinity of accreting neutron stars and stellar black holes (Dubus, this volume), as well as in central energy sources of active galactic nuclei. In these environments, collisions of protons and α -particles (which are the most abundant nuclear species) with ^{12}C and heavier ions can bring nuclei to excited states, which can de-excite by a gamma-ray transition. Gamma-ray emission can also be produced through radiative nuclear capture, for example by the reaction $^{12}\text{C}(p,\gamma)^{13}\text{N}$:



Recently, Bloemen & Bykov (1997) and Bykov *et al.* (1999) proposed that the collective gamma-ray line production from an ensemble of unresolved accreting neutron stars could contribute to the diffuse Galactic emission. They were motivated by COMPTEL observations of the inner Galaxy, which show some evidence for an excess emission with a wide latitudinal distribution ($\sim 20^\circ$ FWHM), that could correspond to the large-scale height of low-mass X-ray binaries (Bloemen & Bykov 1997). However, the expected emission from binary sources crucially depends on the accretion model. Thus, Bildsten *et al.* (1992) predicted very low gamma-ray line fluxes from the brightest neutron star X-ray binaries, if the accreting material is decelerated by Coulomb collisions in the neutron star atmospheres. Indeed, these authors showed that the infalling heavy ions would then thermalize at higher altitudes in the atmosphere than the accreting protons, such that they would be efficiently destroyed by the fast protons, until drifting to the altitude where protons thermalize. On the other hand, Bykov *et al.* (1999) considered an accretion model in which the infalling ions slow down in a *collisionless* shock produced by the outgoing radiation. In this model, heavy ions can coexist with protons and α -particles in the hot postshock plasma for a fraction of second and thermonuclear reactions could then produce an observable gamma-ray line emission. Bykov *et al.* suggested that this emission could be detected with *INTEGRAL* from the nearest sub-Eddington sources.

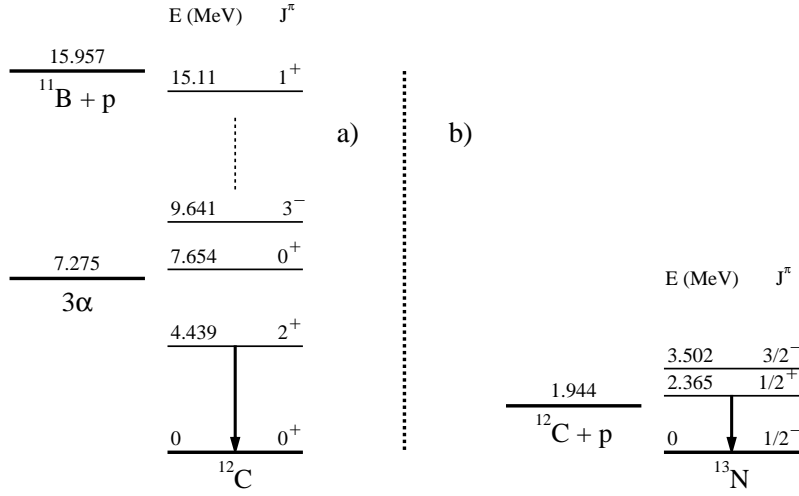


Fig. 9. First nuclear levels of (a) ^{12}C and (b) ^{13}N ($T_{1/2}=9.965$ m). Also shown are (a) the energy thresholds for the breakup of ^{12}C into 3 α -particles (7.275 MeV) and into $^{11}\text{B}+p$ (15.957 MeV) and (b) the energy threshold for the breakup of ^{13}N into $^{12}\text{C}+p$ (1.944 MeV). The reaction $^{12}\text{C}(p,\gamma)^{13}\text{N}$ produces photons of energy (in MeV) $E_\gamma=1.944+E_{cm}$, where E_{cm} is the total kinetic energy of the $^{12}\text{C}+p$ interaction in its center-of-mass rest frame.

One of the strongest gamma-ray lines would then be at 4.438 MeV from de-excitation of the first excited state of ^{12}C (Fig. 9a). This level can be populated by the inelastic scattering reactions $^{12}\text{C}(p,p')^{12}\text{C}_{4.439}^*$ and $^{12}\text{C}(\alpha,\alpha')^{12}\text{C}_{4.439}^*$, as well as by the spallation reactions $^{16}\text{O}(p,p\alpha)^{12}\text{C}_{4.439}^*$ and $^{16}\text{O}(\alpha,2\alpha)^{12}\text{C}_{4.439}^*$ ¹⁰. Other important lines are those resulting from de-excitation of the most abundant heavy nuclei, e.g. at 6.129 MeV from de-excitation of ^{16}O . To illustrate the main characteristics of thermonuclear gamma-ray line production, I discuss in the following the production of the 4.438 MeV line by $p+^{12}\text{C}$ collisions. I also consider the radiative capture reaction (4.1), which produces a line at 2.365 MeV at the resonance energy $E_{cm}=0.421$ MeV (Fig. 9b).

I show in Figure 10 the corresponding thermonuclear reaction rates. For the $^{12}\text{C}(p,p'\gamma_{4.438})^{12}\text{C}$ reaction, I used the cross section tabulated by Kiener et al. (2001) and calculated the thermally-averaged rate from an equation similar to eq. (2.4),

$$\langle \sigma v \rangle = \left(\frac{8}{\pi \mu_{pC}} \right)^{1/2} \frac{1}{(kT_i)^{3/2}} \int_0^\infty E_{cm} \sigma_{pC}(E_{cm}) e^{-E_{cm}/kT_i} dE_{cm}, \quad (4.2)$$

¹⁰ The difference of 1 keV between the energy of the gamma-ray line, 4.438 MeV, and the energy of the first excited state of ^{12}C , 4.439 MeV, is due to the recoil of the ^{12}C nucleus during photon emission.

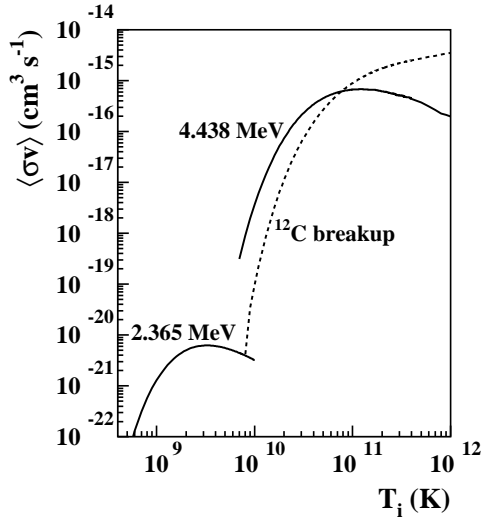


Fig. 10. Maxwellian-averaged reaction rates for $p+^{12}\text{C}$ interactions, as a function of the ion temperature. Solid curves: productions of the 2.365 and 4.438 MeV lines from the reactions $^{12}\text{C}(p,\gamma)^{13}\text{N}$ and $^{12}\text{C}(p,p'\gamma)^{12}\text{C}$, respectively. Dashed curve: destruction of ^{12}C .

which is appropriate for an ion plasma of isothermal temperature $kT_i \ll m_p c^2$ (e.g. Clayton 1983). Here, $\mu_{pC} = m_p m_C / (m_p + m_C)$ is the reduced mass of the $p+^{12}\text{C}$ system, E_{cm} is the total kinetic energy of the reaction in its center-of-mass rest frame and $\sigma_{pC}(E_{cm})$ is the reaction cross section. The rate of the $^{12}\text{C}(p,\gamma_{2.365})^{13}\text{N}$ reaction is obtained from the analytical formula derived by Angulo et al. (1999) for stellar nucleosynthesis purposes, by considering only the contribution of the resonance at $E_{cm} = 0.421$ MeV. We see that the rate of the $^{12}\text{C}(p,p'\gamma_{4.438})^{12}\text{C}$ reaction is several orders of magnitude higher than the one of the radiative capture reaction. This is due to the fact that inelastic scattering reactions are mostly governed by the strong nuclear force, whereas radiative capture reactions are essentially electroweak interactions. However, we also see that the 2.365 MeV line is produced at lower temperature, because the proton capture reaction occurs at lower center-of-mass energy.

The expected width of the 4.438 MeV line depends on the velocity distribution of the excited $^{12}\text{C}^*$. Following Higdon & Lingenfelter (1977), one can neglect the $p+^{12}\text{C}$ reaction kinematics and assume that this distribution is essentially the same as the Maxwell-Boltzmann velocity distribution of unexcited ^{12}C . The line FWHM in keV is then $\sim 9 \times (T_i / 10^8 \text{ K})^{1/2}$, which gives about 90 to 300 keV for T_i between 10^{10} and 10^{11} K. The broadening of the 2.365 MeV line is related to the Maxwellian velocity distribution of the center of mass of $p+^{12}\text{C}$ interactions. One has to consider also the relatively large natural width of the first excited state of ^{13}N , $\Gamma = 32$ keV (Ajzenberg-Selove 1991). In a first approximation, the 2.365 MeV line width can then be estimated as $\text{FWHM} \sim (\Gamma^2 + 2.3 \times 10^{-7} T_i)^{1/2}$, which

gives about 35 to 60 keV for T_i between 10^9 and 10^{10} K (Fig. 10). In addition, lines produced in the vicinity of compact objects can be significantly redshifted, but also broadened if the gravitational potential varies over the emission volume (Shvartsman 1972).

Thermonuclear destruction of the heavy species can lead to a significant reduction in the gamma-ray line production (Guessoum & Gould 1989; Guessoum 1989). To illustrate this point, I show in Figure 10 (dashed curve) the reaction rate for the breakup of ^{12}C by proton impact, which I calculated from eq. (4.2) using for the destruction cross section the fitting formula of Bildsten *et al.* (1992, eq. C4). This cross section has been estimated by subtracting the 4.438 MeV line production cross section from the total $p+^{12}\text{C}$ inelastic reaction cross section, which is justified by the fact that the excited states of ^{12}C above the 4.439 MeV level decay primarily by particle emission¹¹. Let Q be the averaged number of 4.438 MeV gamma-rays emitted in a thermonuclear plasma by a ^{12}C nucleus prior to destruction. We have (Bildsten *et al.* 1992)

$$Q \leq \frac{\langle \sigma v \rangle_\gamma}{\langle \sigma v \rangle_d}, \quad (4.3)$$

where $\langle \sigma v \rangle_\gamma$ and $\langle \sigma v \rangle_d$ are the reaction rates for gamma-ray production and ^{12}C destruction, respectively. Thus, we see from Figure 10 that $Q \ll 1$ for $T_i \gg 10^{11}$ K, which merely illustrates that destruction, rather than 4.438 MeV line emission, is by far the most probable outcome for ^{12}C nuclei in such very high-temperature plasmas. Note that photon- and electron-induced reactions can also destroy heavy nuclei. However, Guessoum & Gould (1989) estimated that these processes should generally be negligible as compared with breakup by proton collisions.

As a conclusion, a near future observation of thermonuclear gamma-ray lines is uncertain, because the accreting heavy ions could be rapidly destroyed either by thermal or nonthermal processes. However, the breakup of ^4He and heavier nuclei should be accompanied by a copious liberation of neutrons, that may eventually recombine with protons to produce a gamma-ray line emission at 2.22 MeV (§ 4.3). This line could be produced within the high-temperature plasma near the compact object (Bildsten *et al.* 1993) or in the atmosphere of the companion star (Jean & Guessoum 2001). In fact, it may be the best gamma-ray line candidate for high-energy accreting sources.

4.2 Nonthermal gamma-ray line production from accelerated ion interactions

The interaction of accelerated nuclei (typically >1 MeV/nucleon) with ambient matter can produce a wealth of gamma-ray lines with energies ranging from tens of keV to about 20 MeV. This nonthermal gamma-ray line emission is often observed from the Sun during strong solar flares (e.g. Vestrand *et al.* 1999) and it has furnished valuable information on solar ambient abundances, density and

¹¹ An exception is the 15.11 MeV level, which, because of conservation of isotopic spin, decays essentially by γ -ray emission (Fig. 9a).

temperature, as well as on accelerated particle composition, spectra and transport in the solar atmosphere (e.g. Ramaty & Mandzhavidze 2000; Share & Murphy 2001). Nonthermal gamma-ray line emission is also expected from various astrophysical sites in which ion acceleration is believed to occur, such as accreting compact stellar objects, supernova remnants and active galactic nuclei. Interactions of Galactic cosmic-ray ions with interstellar matter should produce a diffuse emission that might be observed in the near future. These observations would then shed new light on the global physical structure of the interstellar medium and on the sources of cosmic rays below 100 MeV/nucleon, that are not detected near Earth because of the solar modulation.

The most comprehensive treatment of nuclear de-excitation gamma-ray line emission was performed by Ramaty *et al.* (1979). The authors took into account more than 150 reactions leading to the production of an excited nucleus and evaluated their cross sections from laboratory measurements combined with nuclear physics theory. Figure 11 shows a gamma-ray line spectrum which I calculated with the corresponding computer code¹². I have considered the same steady state, thick target interaction model as for the nonthermal X-ray emission shown in Figure 8, in particular with the same composition (CRS) and source spectrum (eq. 3.7) for the accelerated ions. The luminosity of the calculated gamma-ray line emission is

$$L_{\gamma} = \int_{0.1 \text{ MeV}}^{8 \text{ MeV}} E_{\gamma} \frac{dQ}{dE_{\gamma}}(E_{\gamma}) dE_{\gamma} = 1.1 \times 10^{-5} \text{ erg s}^{-1} , \quad (4.4)$$

which is comparable to the calculated X-ray luminosity ($L_X < 4.8 \times 10^{-5} \text{ erg s}^{-1}$, see Fig. 8). This should generally be the case, except if the accelerated ion spectrum is very soft: a high population of low-energy ions ($\sim 1 \text{ MeV/nucleon}$) can produce nonthermal soft X-rays without producing a significant gamma-ray line emission.

We see in Figure 11 a combination of broad line features from de-excitations of fast heavy ions, narrower lines from gamma-ray transitions in heavy nuclei excited by energetic protons and α -particles and very narrow lines (dotted lines) from spallation-produced long-lived radionuclei, which can come essentially to rest in the ambient medium before decaying to an excited state of their daughter nucleus. In addition, the prominent broad line feature at $\sim 0.45 \text{ MeV}$ is mainly produced by the interactions of α -particles with ambient ^4He .

All these lines are superimposed on a continuum-like emission (dashed curve), which is due to a large number of unresolved gamma-ray lines, mostly arising from cascade transitions in high-lying levels of heavy nuclei. Ramaty *et al.* (1979) estimated the intensity and the energy distribution of this unresolved emission from the data of Zobel *et al.* (1968). These authors measured the total production of gamma-rays of energies $> 0.7 \text{ MeV}$, in interactions of protons and α -particles with

¹² The code has been recently updated by taking into account new laboratory data allowing improved theoretical evaluations of many cross sections (Kozlovsky *et al.* 2002). It can be downloaded from the URL: <http://lheawww.gsfc.nasa.gov/users/ramaty/ViewPubs/ramaty.html> .

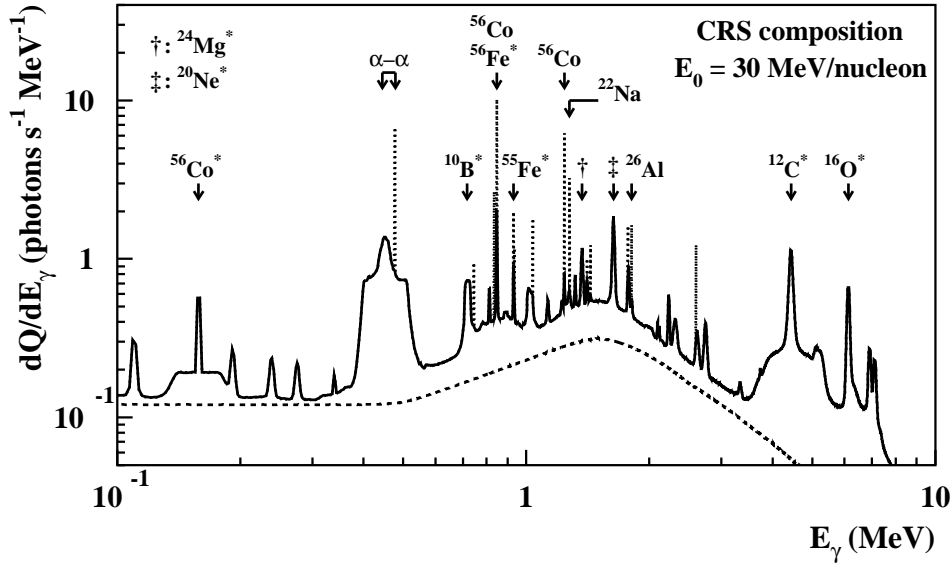


Fig. 11. Calculated gamma-ray line emission produced by accelerated ions with the same composition (CRS) and source spectrum as in Figure 8, also interacting in a neutral ambient medium of solar composition. The calculation is normalized to the same power of 1 erg s^{-1} deposited by the accelerated particles in the interaction region. The dashed curve shows the estimated contribution from all unresolved gamma-ray lines in ions heavier than ^{16}O (see text). The very narrow dotted lines are from the decay of long-lived radionuclides. The arrows point to the lines which are mentioned in the text. The prompt lines are labelled with the excited nuclei from which the gamma-rays are emitted (e.g. $^{12}\text{C}^*$), whereas the delayed lines are labelled with the parent long-lived radioisotopes (e.g. ^{26}Al). The so-called $\alpha-\alpha$ line feature is mainly produced by $\alpha+\alpha$ fusion reactions (see also Fig. 12).

complex nuclei, at laboratory energies $>10 \text{ MeV/nucleon}$. They found that for target nuclei heavier than O, the resolvable lines from de-excitation of the low-lying nuclear levels can account for only a fraction of the total gamma-ray production. In the spectrum of Figure 11, however, the unresolved component produces about half of the total gamma-ray emission below 3 MeV. New experiments could allow to specify the importance of this emission.

The broad lines tend to overlap, such that only few well-defined features from energetic heavy ions can be distinguished in the gamma-ray spectrum. It is the case of the broad line feature from fast $^{12}\text{C}^*$, centered at 4.4 MeV (Fig. 11) with FWHM of $\sim 1.5 \text{ MeV}$, which is produced by interactions of accelerated ^{12}C and ^{16}O with ambient H and He. An other example is furnished by the broad line centered at 0.158 MeV with FWHM of $\sim 50 \text{ keV}$, which is due to the de-excitation of the first excited state of ^{56}Co , populated by the reaction in reverse kinematics

${}^1\text{H}({}^{56}\text{Fe}, {}^{56}\text{Co}^*)n$.

Intense narrow lines are due to excitations of low-lying nuclear levels in abundant ambient ions, e.g. at 0.847 MeV from ${}^{56}\text{Fe}^*$, 1.37 MeV from ${}^{24}\text{Mg}^*$, 1.63 MeV from ${}^{20}\text{Ne}^*$, 4.44 MeV from ${}^{12}\text{C}^*$ and 6.13 MeV from ${}^{16}\text{O}^*$. Other important narrow lines are those arising from transitions in the spallation products of abundant ambient nuclei, e.g. at 0.718 MeV from ${}^{10}\text{B}^*$, which is produced by the spallation of ambient ${}^{12}\text{C}$ and ${}^{16}\text{O}$, and at 0.931 MeV from ${}^{55}\text{Fe}^*$, which is essentially produced by the reaction ${}^{56}\text{Fe}(p,pn){}^{55}\text{Fe}^*$. The narrow lines produced in a gaseous ambient medium are generally broadened by the recoil velocity of the excited nucleus and their FWHM is about 0.5-5% of the transition energy. However, some lines produced in interstellar dust grains can be very narrow, because some of the excited nuclei can stop in solid materials before emitting gamma-rays¹³ (Lingenfelter & Ramaty 1977). It requires that (i) the mean life time of the excited nuclear level or of its radioactive nuclear parent is longer than the slowing down time of the excited nucleus in the grain material and (ii) the mean distance from the site of the nuclear interaction to the grain edge is higher than the stopping range of the excited nucleus in the grain. The most promising candidates are from the de-excitation of the levels of ${}^{56}\text{Fe}$ at 0.847 MeV ($T_{1/2}=6.1$ ps) and 1.238 MeV ($T_{1/2}=640$ fs), of ${}^{24}\text{Mg}$ at 1.37 MeV ($T_{1/2}=1.35$ ps), of ${}^{28}\text{Si}$ at 1.78 MeV ($T_{1/2}=475$ fs) and of ${}^{16}\text{O}$ at 6.13 MeV ($T_{1/2}=18.4$ ps). Most of the interstellar Fe, Mg and Si, which are refractory elements, could be contained in dust grains, whereas about half of the interstellar O could be in grains (e.g. Savage & Sembach 1996). The detection of these very narrow lines, maybe with the *INTEGRAL* spectrometer (SPI), would provide unique information on the composition, size and spatial distribution of the interstellar grains.

Both the broad and the narrow lines could in principle have complex profiles that generally depend on the composition, energy and angular distributions of the accelerated particles¹⁴, the composition of the ambient medium and the mechanism of the nuclear reactions producing the excited nuclei. In particular, the detailed calculation of line shapes requires the knowledge of the angular and energy distributions of the recoil nuclei and the angular distribution of the emitted gamma-rays. Ramaty *et al.* (1979) estimated the shapes of the various lines from a limited number of available laboratory data together with simplifying theoretical assumptions. More recent works have shown that fine spectroscopic analyses of the gamma-ray line profiles could give valuable information on the directionality of the accelerated particles in the interaction region (Kiener *et al.* 2001 and references therein).

In Figure 11, the most intense narrow lines from spallation-produced radionuclides are at 0.478 MeV from the decay of ${}^7\text{Be}$ ($T_{1/2}=53.3$ d), at 0.847 and 1.238 MeV from the decay of ${}^{56}\text{Co}$ ($T_{1/2}=77.3$ d) and at 1.275 MeV from the decay of ${}^{22}\text{Na}$

¹³ This is not taken into account in the present calculations, for which I assumed that the ambient medium is devoid of dust grains.

¹⁴ In the updated nuclear de-excitation line code of Ramaty *et al.*, the accelerated particles are assumed to have an isotropic distribution in the interaction region.

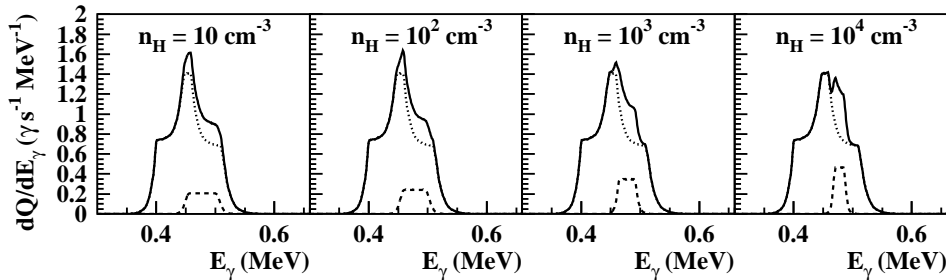


Fig. 12. Profiles of the gamma-ray line emission at ~ 0.45 MeV, for 4 values of the H density in the interaction region. The total emission (solid curves) is the sum of the prompt lines from the reactions ${}^4\text{He}(\alpha, n\gamma_{0.429}){}^7\text{Be}$ and ${}^4\text{He}(\alpha, p\gamma_{0.478}){}^7\text{Li}$ (dotted curves) and the delayed line at 0.478 MeV from ${}^7\text{Be}$ decay (dashed curves).

($T_{1/2}=2.6$ y). These lines are very narrow only if the density of the ambient medium is high enough for the radionuclides to come essentially to rest prior to decay. The line at 1.809 MeV from ${}^{26}\text{Al}$ decay should generally be very narrow, because the time to stop energetic (<100 MeV/nucleon) ${}^{26}\text{Al}$ in a medium of ~ 1 H-atom cm^{-3} is shorter than its half-life ($T_{1/2}=7.4\times 10^5$ y). But ${}^7\text{Be}$ ions, which are mostly produced by the reaction ${}^4\text{He}(\alpha, n){}^7\text{Be}$ with recoil energy >2 MeV/nucleon, stop in a medium with solar abundances in less than 53.3 days only if the H density exceeds 10^5 cm^{-3} .

Figure 12 shows detailed profiles of the gamma-ray emission at ~ 0.45 MeV for lower values of the ambient H density (Tatischeff *et al.* 2001). The delayed line at 0.478 MeV from ${}^7\text{Be}$ decay is superimposed on a prompt emission from the reactions ${}^4\text{He}(\alpha, n\gamma_{0.429}){}^7\text{Be}$ and ${}^4\text{He}(\alpha, p\gamma_{0.478}){}^7\text{Li}$. The two prompt lines merge (for the assumed isotropic distribution of energetic α -particles) thus producing this characteristic emission feature, whose importance in gamma-ray astrophysics was first pointed out by Kozlovsky & Ramaty (1974). We see that the width of the delayed line decreases as the H density increases, because ${}^7\text{Be}$ ions decay at lower energies in a denser propagation region. This provides a potential density measurement, which could allow, in particular, to determine if low-energy cosmic-ray ions can penetrate into the core of interstellar molecular clouds.

In summary, interactions of energetic particles with ambient material produce a great variety of nuclear de-excitation lines, that could provide a unique tool to study the acceleration processes at work in the Galaxy and beyond, and also to examine the ultimate nature of the interaction regions. In particular, observations of diffuse Galactic emission would permit the first measurements of the isotopic composition of the interstellar medium, independent of the ionization and molecular states of its constituents.

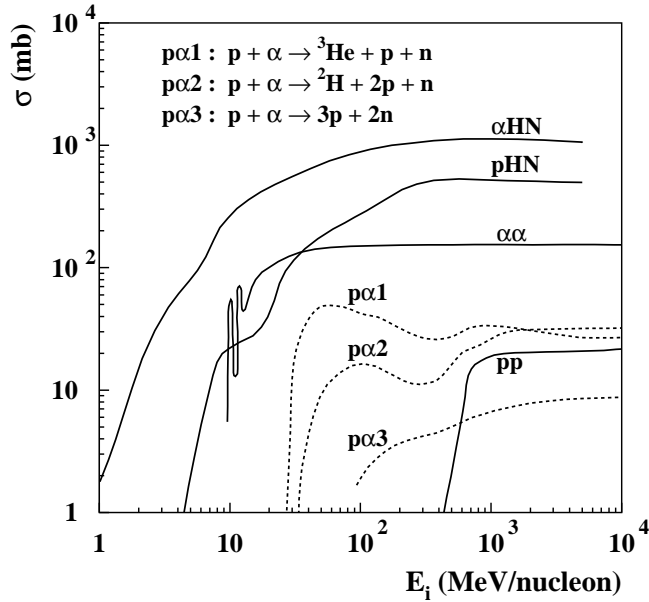


Fig. 13. Neutron production cross sections in units of millibarn $\equiv 10^{-27} \text{ cm}^{-2}$, as a function of the proton or α -particle bombarding energy. Here, pp , $p\alpha$, $\alpha\alpha$, pHN and αHN indicate neutron production in proton–hydrogen, proton–helium, alpha particle–helium, proton–heavy nuclei and alpha particle–heavy nuclei interactions, respectively. The cross sections of the three neutron-producing reactions in proton–helium interactions are shown separately (dashed curves). The pHN and αHN reaction cross sections take into account all isotopes equal to or heavier than ^{12}C (see text). All the cross sections include the neutron multiplicity.

4.3 The radiative capture of neutrons

Free neutrons can be produced by the breakup of all isotopes equal to or heavier than ^2H , either by thermonuclear or nonthermal reactions. Their subsequent radiative capture by ambient nuclei can produce many specific gamma-ray lines, among which the line at 2.22 MeV from the reaction $^1\text{H}(n,\gamma)^2\text{H}$ is expected to be the strongest in most astrophysical sites.

I show in Figure 13 the cross section for important neutron-producing reactions. The pHN and αHN reaction cross sections are from Hua & Lingenfelter (1987a; see also Ramaty *et al.* 1975). They are defined as

$$\sigma_{pHN} = \frac{1}{\sum_k a_k} \sum_i a_i \sigma_{pi} \quad (4.5)$$

$$\sigma_{\alphaHN} = \frac{1}{\sum_k a_k} \sum_i a_i \sigma_{\alpha i} \quad (4.6)$$

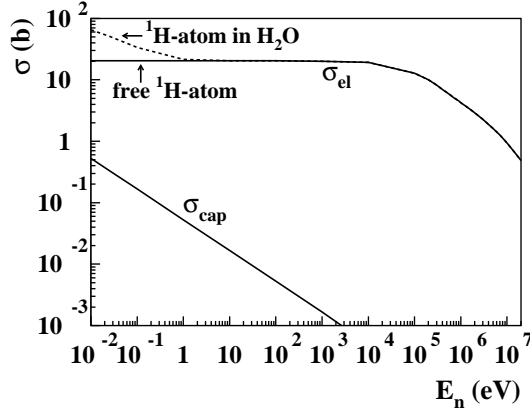


Fig. 14. Cross sections for the elastic scattering of a neutron on a free ${}^1\text{H}$ -atom and on a ${}^1\text{H}$ -atom contained in a water molecule (dashed curve), and for the radiative capture reaction ${}^1\text{H}(n,\gamma){}^2\text{H}$, as a function of the neutron energy (from Horsley 1966). The radiative capture cross section satisfies $\sigma_{cap}(E_n)=2.44\times 10^{-6}/\beta_n$ (in b) for $E_n<1$ keV, where β_n is the neutron velocity relative to that of light.

where a_i is the solar abundance of isotope i with respect to ${}^1\text{H}$, σ_{pi} (resp. $\sigma_{\alpha i}$) is the cross section for neutron production in collisions of protons (resp. α -particles) with isotope i and the summations are over all isotopes equal to or heavier than ${}^{12}\text{C}$ ($\sum_k a_k=1.6\times 10^{-3}$). The cross sections of the pp , $p\alpha$ and $\alpha\alpha$ reactions are from Murphy *et al.* (1987; see also Meyer 1972). These reactions should generally be the dominant neutron-producing processes in interactions of accelerated particles of energy >10 MeV/nucleon and in thermonuclear plasmas. However, spallation of heavy nuclei plays an important role in solar flares, because the accelerated ions have generally a rapidly decreasing energy distribution.

Shown in Figure 14 are cross sections for $n+\text{H}$ interactions. We see that the neutrons have a much larger probability to scatter on ambient ${}^1\text{H}$ -atoms than to be captured. They lose on average about half of their kinetic energy in each elastic scattering. Thus, most of them get thermalized before being possibly captured, if they haven't decayed ($n\rightarrow p+e^-+\bar{\nu}_e$) or escaped from the interaction region. In a medium of H density n_H , the mean time for radiative capture is given by

$$\tau_{cap} = \frac{1}{n_H \sigma_{cap} \beta_n c} \quad (4.7)$$

$$= \frac{1.4 \times 10^{19} \text{ s}}{n_H (\text{cm}^{-3})} \text{ for } E_n < 1 \text{ keV} , \quad (4.8)$$

as $\sigma_{cap}(E_n)=2.44\times 10^{-30}/\beta_n$ (in cm^2) for $E_n<1$ keV (Fig. 14). This characteristic time must be compared with the mean time for neutron decay:

$$\tau_{dec} = \frac{T_{1/2}}{\ln(2)} = 886 \text{ s}, \quad (4.9)$$

where $T_{1/2}=613.92\pm 0.55$ s is the neutron half-life (Groom *et al.* 2000). Thus, significant gamma-ray line emission at 2.22 MeV can only be produced in an ambient medium of H density exceeding $\sim 10^{16}$ cm $^{-3}$, i.e. in a *stellar environment*. The line should generally be narrow if the only broadening mechanism is thermal. If it is the case, its FWHM exceeds the energy resolution of a Germanium detector (~ 2.5 keV at 2.2 MeV) only if the ambient medium temperature is $\gtrsim 5\times 10^6$ K.

As pointed out by Wang & Ramaty (1974), ambient ^3He can constitute an important non-radiative sink for the neutrons. Indeed, the cross section for the reaction $^3\text{He}(n,p)^3\text{H}$ has the same form at low energies as that of the $^1\text{H}(n,\gamma)^2\text{H}$ reaction ($\sigma(E_n) \propto 1/\beta_n$), but is $\sim 1.6\times 10^4$ times larger, which is to be compared with the $^1\text{H}/^3\text{He}$ solar abundance ratio, 7.23×10^4 (Anders & Grevesse 1989). In fact, this coincidence has allowed an original determination of the ^3He photospheric abundance, from observations of the 2.22 MeV line produced in solar flares (Hua & Lingenfelter 1987b).

The COMPTEL all-sky survey at 2.22 MeV revealed one point-like feature (GRO J0332-87) at the Galactic coordinates $(\ell,b)=(300.5^\circ,-29.6^\circ)$ (McConnell *et al.* 1997; Schönfelder *et al.* 2000). The most interesting known source in the COMPTEL location error box is RE J0317-853, which is one of the hottest ($\approx 50,000^\circ$ K) and most highly magnetized (≈ 340 MG) white dwarfs, residing at a distance of only ~ 35 pc. Observations with *INTEGRAL* are expected to provide a new insight into the origin of this yet mysterious emission.

5 Gamma- and X-ray lines from stellar nucleosynthesis

Observations of gamma-ray lines produced by the decay of radioisotopes synthesized in stars have long been recognized as a powerful tool for studying the nucleosynthesis processes at work in stellar interiors and explosions (Clayton 1982 and references therein; Knödlseher, this volume). However, among the hundreds of potential radioactive emitters of gamma-ray lines, only a few of them are suitable for astronomical observations. First, nucleosynthesis sites are generally optically thick to gamma-rays, such that the appropriate radioisotopes must have a sufficiently long half-life (typically $T_{1/2}>1$ day) so as to decay only after having left the dense production environment. Additionally, their production yields must be high enough for the decay activities to be observable by gamma-ray instruments, which, in the present state of the gamma-ray line astronomy, practically excludes all the radioisotopes beyond the Fe peak.

Table 1 lists the most important cosmic radioactivities for gamma-ray line observations. The astrophysical sites in which these isotopes are synthesized are discussed in the review paper of Diehl & Timmes (1998). The nuclear data are from Firestone (1996, and references therein for the ϵ - β^+ decay branchings), except for the nuclei of mass number $A=44$, 56 and 57, for which I used the more recent data evaluations of Cameron & Singh (1999), Junde (1999) and Bhat (1998), respectively. The half-life of the radioisotopes listed in the Table should be compared with the characteristic time scale between two nucleosynthesis events which produced them in the Galaxy, ~ 1 -2 weeks for novae, ~ 40 yr for CCSN and ~ 300 yr

Table 1. Star-produced radioisotopes relevant to gamma-ray line astronomy.

Iso- tope	Production sites^a	Decay chain^b	Half- life^c	γ-ray energy (keV) and intensity^d
⁷ Be	Nova	⁷ Be $\xrightarrow{\epsilon}$ ⁷ Li*	53.3 d	478 (0.11)
⁵⁶ Ni	SNIa, CCSN	⁵⁶ Ni $\xrightarrow{\epsilon}$ ⁵⁶ Co*	6.075 d	158 (0.99), 812 (0.86)
		⁵⁶ Co $\xrightarrow{\epsilon(0.81)}$ ⁵⁶ Fe*	77.2 d	<u>847</u> ^e (1), <u>1238</u> (0.67)
⁵⁷ Ni	SNIa, CCSN	⁵⁷ Ni $\xrightarrow{\epsilon(0.56)}$ ⁵⁷ Co*	1.48 d	1378 (0.82)
		⁵⁷ Co $\xrightarrow{\epsilon}$ ⁵⁷ Fe*	272 d	<u>122</u> (0.86), <u>136</u> (0.11)
²² Na	Nova	²² Na $\xrightarrow{\beta^+(0.90)}$ ²² Ne*	2.61 y	<u>1275</u> (1)
⁴⁴ Ti	SNIa, CCSN	⁴⁴ Ti $\xrightarrow{\epsilon}$ ⁴⁴ Sc*	60.0 y	<u>68</u> (0.93), <u>78</u> (0.96)
		⁴⁴ Sc $\xrightarrow{\beta^+(0.94)}$ ⁴⁴ Ca*	3.97 h	<u>1157</u> (1)
²⁶ Al	CCSN, WR AGB, Nova	²⁶ Al $\xrightarrow{\beta^+(0.82)}$ ²⁶ Mg*	7.4·10 ⁵ y	<u>1809</u> (1)
⁶⁰ Fe	CCSN	⁶⁰ Fe $\xrightarrow{\beta^-}$ ⁶⁰ Co*	1.5·10 ⁶ y	59 (0.02 ^f)
		⁶⁰ Co $\xrightarrow{\beta^-}$ ⁶⁰ Ni*	5.27 y	1173 (1), 1332 (1)

^a Sites which are believed to produce observable γ -ray line emission. Nova: classical nova; SNIa: thermonuclear supernova (type Ia); CCSN: core-collapse supernova; WR: Wolf-Rayet star; AGB: asymptotic giant branch star.

^b ϵ : orbital electron capture. When an isotope decays by a combination of ϵ and β^+ emission, only the most probable decay mode is given, with the corresponding fraction in parenthesis.

^c Half-lives of the isotopes decaying by ϵ are for the neutral atoms (see text).

^d Number of photons emitted in the γ -ray line per radioactive decay.

^e The underlined γ -ray lines are those for which a positive detection has been reported at the time of writing.

^f It is noteworthy that the first excited (isomeric) state of ⁶⁰Co at 59 keV decays with 98% probability by the emission of a conversion electron.

for SNIa (e.g. Prantzos 1999 and references therein). Thus, we see that we expect the decays of the long-lived ²⁶Al and ⁶⁰Fe nuclei to produce diffuse gamma-ray line emissions, resulting from the superposition of numerous Galactic sources. On the other hand, the gamma-ray line activities of ⁷Be, ⁵⁶Ni, ⁵⁷Ni and ⁴⁴Ti should be observed in individual transient events. The case of ²²Na is in a way intermediary: the line emission at 1.275 MeV could be observed from nearby individual ONE novae (<1.1 kpc with SPI, Hernanz et al. 2001), but also from a broad region towards the Galactic center, resulting from the cumulated production of few tens of active sources. Evidence for this latest unresolved emission has recently been reported by the COMPTEL team (Iyudin *et al.* 2002).

In Table 1, six of the radioisotopes decay mainly or exclusively by orbital electron capture (ϵ). As pointed out by Mochizuki *et al.* (1999) for ⁴⁴Ti, one

has to be cautious when deducing the production yields of these isotopes from the delayed observations of their gamma-ray activities, since their decay rates depend on their ionization states. Thus, in the interstellar medium, fully ionized ϵ -radioisotopes can only decay by highly improbable nuclear electron capture from continuum states, such that they are almost stable as compared with the age of the universe¹⁵. Mochizuki *et al.* (1999) suggested that the ionization of ^{44}Ti behind the reverse shock of the Cas A supernova remnant (SNR) could have significantly reduced its decay rate, thus leading to a lower mass of ejected ^{44}Ti than previously inferred from the detected 1.157 MeV line flux. However, a more realistic model for the ejecta shows that the effect may not exceed a few percent (Laming 2002).

The decay of an ϵ -radioisotope can also produce X-ray line emission, when the electron vacancy in the daughter atom (primarily in its K-shell) is filled by a radiative transition¹⁶. Leising (2001) has recently examined the exciting possibility of detecting cosmic radioactivities in X-rays. Many of them are not gamma-ray line emitters, because they decay directly to the ground state of their daughter nucleus. The author listed 17 potentially important ϵ -radioisotopes, among which the most promising for detection are ^{55}Fe ($T_{1/2}=2.73$ yr), ^{44}Ti ($T_{1/2}=60$ yr), ^{59}Ni ($T_{1/2}=7.6\times 10^4$ yr) and ^{53}Mn ($T_{1/2}=3.74\times 10^6$ yr). The ϵ decay of ^{55}Fe could be observed through the emission of the Mn $K\alpha$ line, from very young SNRs such as SN1987A. The X-ray line emission which accompanies the ^{44}Ti decay should be hunted for in the two SNRs from which gamma-ray line emission at 1.157 MeV has already been observed, Cas A and RX J0852-4622. The detection of this X-ray line emission would constitute an interesting complement to the gamma-ray line measurements, because it would allow to determine the present ionization state of Ti in the two SNRs. Finally, the decays of ^{59}Ni and ^{53}Mn , producing $K\alpha$ lines at 6.92 and 5.41 keV, respectively, could be observed from very close and reasonably young (i.e. not too extended) SNRs and also as diffuse Galactic emissions¹⁷. As Leising pointed out, it could be difficult to distinguish the electron capture line emission from astrophysical sources which are generally expected to

¹⁵ This is not the case in stellar interiors because of the much higher density of continuum electrons. For example, the half-life of ^7Be against capture of free electrons in the core of the Sun is ≈ 90 d (Bahcall & Moeller 1969), which is by coincidence comparable to the measured value for neutral atoms.

¹⁶ The adjustment of the nucleus is generally much faster than the atomic rearrangement, such that the atomic transition usually occurs in the daughter element.

¹⁷ A diffuse emission in the Co $K\alpha$ line at 6.92 keV is also expected from the decay chain $^{60}\text{Fe} \xrightarrow{\beta^-} ^{60}\text{Co}_{59\text{ keV}}^* \xrightarrow{IT} ^{60}\text{Co}$ (IT: internal transition), since the de-excitation of $^{60}\text{Co}_{59\text{ keV}}^*$ is essentially due to the conversion of a K-shell electron (see Table 1). The expected Galactic flux is

$$F_X = F_\gamma \frac{\alpha(K)}{1+\alpha} \omega_{\text{Co}}^{K\alpha} \cong 1.8 \times 10^{-5} \text{ photons s}^{-1} \text{ cm}^{-2}, \quad (5.1)$$

where $F_\gamma \cong 6.5 \times 10^{-5} \text{ } \gamma \text{ s}^{-1} \text{ cm}^{-2}$ is the predicted flux for the 1.173 MeV line from ^{60}Co decay (Timmes & Woosley 1997), $\alpha=48$ and $\alpha(K)=40$ are the total and K-shell conversion coefficients for the 59 keV transition (King 1993) and $\omega_{\text{Co}}^{K\alpha}=0.33$ is the $K\alpha$ fluorescence yield for Co. In comparison, Leising (2001) predicted that the decay of ^{59}Ni should produce a 6.92 keV line flux from the central steradian of the Galaxy of $\sim 1.7 \times 10^{-4} \text{ photons s}^{-1} \text{ cm}^{-2}$.

be very luminous in X-rays. In particular, detailed models of SNRs are required to determine if the expected lines could be unambiguously identified among the other thermal and nonthermal X-ray line emissions. However, one can reasonably hope that in a few cases, the clear detection of X-ray lines from cosmic radioactivities will constitute an important complement to the gamma-ray line studies of stellar nucleosynthesis.

6 Positron annihilation radiation

Positron-electron annihilation radiation can be produced in a variety of astrophysical sites. The diffuse Galactic emission at 511 keV is the brightest gamma-ray line of cosmic origin. It is produced by the steady-state annihilation of $\sim 1.4\text{--}4.3 \times 10^{43}$ positrons s^{-1} (depending on the spatial distribution of the emission, Kinzer *et al.* 2001). A large fraction of these positrons could result from the β^+ decay of ^{56}Co and ^{44}Sc (synthesized as ^{56}Ni and ^{44}Ti in supernovae, see Table 1), with a smaller contribution from the β^+ decay of ^{26}Al (Chan & Lingenfelter 1993; Dermer & Murphy 2001). Milne *et al.* (2002) have recently estimated that these three isotopes could supply 30-50% of the Galactic positrons. The decay of π^+ and radioisotopes produced by cosmic-ray interactions in the interstellar medium could make an additional contribution of a few percent (e.g. Ramaty & Lingenfelter 1979).

Positrons are also produced in classical novae, from the decay of radioisotopes synthesized during the thermonuclear runaway. The main β^+ -radionuclei synthesized in novae are ^{13}N ($T_{1/2}=9.965$ min), ^{18}F ($T_{1/2}=109.8$ min), ^{22}Na ($T_{1/2}=2.61$ h) and ^{26}Al ($T_{1/2}=7.4 \times 10^5$ y). The decay of the latter two isotopes could inject a small but non-negligible amount of positrons in the interstellar medium, but ^{13}N and ^{18}F have too short half-lives, so that most of the positrons should annihilate in the relatively dense material ejected by the nova explosion. The resulting gamma-ray emission could be detected with SPI from relatively nearby novae during the first day after the explosion¹⁸ (Hernanz *et al.* 2001).

Positron production can also occur in accreting compact objects, from the pair production reaction $\gamma + \gamma \rightarrow e^- + e^+$, from the materialization of photons in strong magnetic fields $\gamma + \vec{B} \rightarrow e^- + e^+ + \vec{B}$ and from other less important processes such as $\gamma + X \rightarrow e^- + e^+ + X$, where $X \equiv e^-$ or nucleus. A significant fraction of these positrons could annihilate near the compact objects, thus producing a localized and possibly time-variable emission. The annihilation radiation from relativistic plasmas is discussed by Marcowith (this volume). Here, I consider the emission produced by the injection of nonthermal positrons in various astrophysical environments.

Important processes leading to gamma-ray emission from positron annihilation are shown in Figure 15 (see Guessoum *et al.* 1997 for discussion of the various

¹⁸ The detectability of this emission crucially depends on the uncertain rates of the reactions $^{18}\text{F}(p,\gamma)^{19}\text{Ne}$ and $^{18}\text{F}(p,\alpha)^{15}\text{O}$, which are responsible for the thermonuclear destruction of ^{18}F (Coc *et al.* 2000).

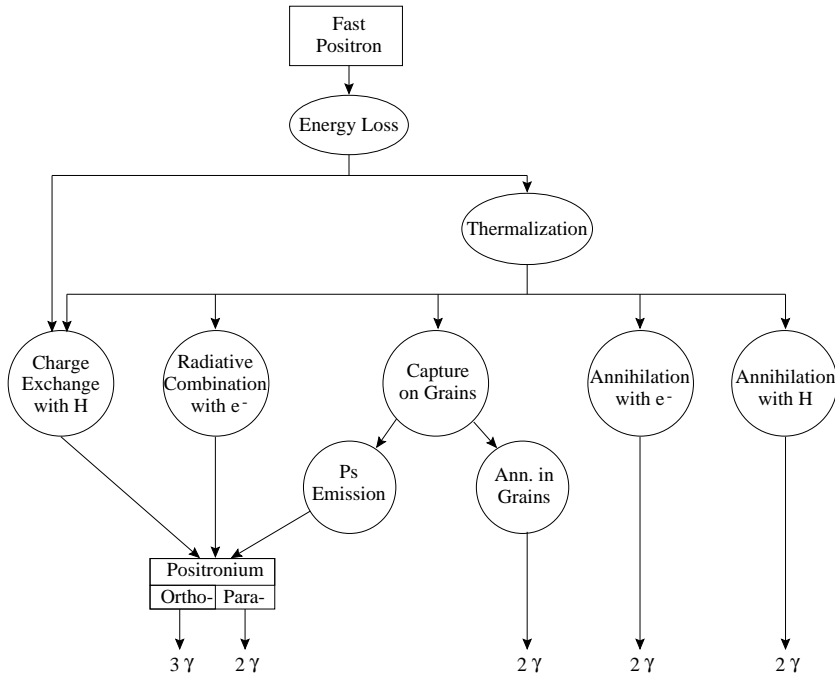


Fig. 15. Main processes leading to gamma-ray emission from positron annihilation (adapted from Guessoum *et al.* 1991, fig. 1).

processes and update of the cross sections). Positrons produced by the decay of radioactive nuclei have initial kinetic energies typically ranging from several hundred keV to few MeV. They slow down mainly by Coulomb interactions with free electrons and by excitations and ionizations of neutral atoms, and their characteristic slowing-down time is $\sim 10^5/n$ years, where n is the ambient medium density in units of cm^{-3} (Guessoum *et al.* 1991). Positrons produced by other processes generally have higher initial energies. Having lost the bulk of its kinetic energy, a positron can either form a positronium (Ps) atom in flight by charge exchange with an atom or a molecule (at $\lesssim 50$ eV in neutral H or H₂, Bussard *et al.* 1979) or become thermalized with the free electrons. Thermal positrons either annihilate directly with free or bound electrons or form Ps atoms through radiative recombination and charge exchange (Fig. 15). As first pointed out by Zurek (1985), interstellar dust could play a significant role in annihilation of thermal positrons despite its low abundance, since its projected surface area ($\sim 10^{-21}$ cm² per Galactic H-atom) can be larger than the cross sections for the other processes leading to positron annihilation. Collisions of thermal positrons with dust grains can lead to the reflection of the positrons from the grains, to the annihilation of the positrons within the grains and to the formation and subsequent escape of Ps atoms back to the gas. The contribution of these processes to gamma-ray emission crucially

depends on the grain properties, including their compositions, sizes, charges and abundances in the ambient medium.

The positronium atom, which is the simplest hydrogen-like system, is preferentially formed in the state of principal quantum number $n=1$, either as a triplet (3S_1) in which the spins of the electron and positron are parallel, or as a singlet (1S_0) in which they are antiparallel¹⁹. These states are called, respectively, orthopositronium and parapositronium, by analogy with the spectral designations for hydrogen. Parapositronium annihilates with a lifetime $\tau_p=1.25\times 10^{-10}$ s into two photons of 511 keV in its rest frame, but orthopositronium decays with $\tau_o=1.4\times 10^{-7}$ s into three photons, which form a characteristic continuum at energies below 511 keV (Ore & Powell 1949). Ps atoms can be quenched before annihilation if the ambient medium density is $\gtrsim 10^{13}$ cm³.

Let I_{e^+} be the total number of positrons which annihilate in a given source, and $I_{2\gamma}$ and $I_{3\gamma}$ the number of photons emitted from this source in the 511 keV line and in the ortho-Ps continuum, respectively. Since the probability for formation of the lepton atom in the triplet state is three times the probability for its formation in the singlet state, we have

$$I_{2\gamma} = I_{e^+} \times [2 \times (1/4) \times f_{Ps} + 2 \times (1 - f_{Ps})] \quad (6.1)$$

$$\text{and } I_{3\gamma} = I_{e^+} \times 3 \times (3/4) \times f_{Ps} , \quad (6.2)$$

where f_{Ps} is the fraction of positrons that annihilate via Ps formation. Combining these two equations gives f_{Ps} in terms of the observable quantity ($I_{2\gamma}/I_{3\gamma}$):

$$f_{Ps} = \frac{2}{2.25(I_{2\gamma}/I_{3\gamma}) + 1.5} . \quad (6.3)$$

To illustrate how an observation of the 511 keV line profile and the determination of f_{Ps} can provide unique information on the annihilation environment, I show in Figure 16 calculated spectra of the radiation produced by positron annihilation in the four phases of the interstellar medium. I used equation (9) of Guessoum *et al.* (1991) with the rates of the various processes and the corresponding line widths given in that paper, except for the widths of the lines produced by radiative recombination and direct annihilation of thermal positrons, for which I used the more accurate results of Crannell *et al.* (1976; see Guessoum *et al.* 1997). For simplicity, I neglected the processes involving interstellar dust.

We see in panel (a) that in the cold phase, the line is relatively broad and the fraction of positrons which annihilate via Ps formation is high. Indeed, in this neutral environment, most of the nonthermal positrons form Ps in flight by charge exchange and the immediate annihilation of para-Ps produces a broad line (6.4 keV FWHM, Brown *et al.* 1984). On this component is superimposed a

¹⁹ The formation of a Ps atom in an excited state can produce a Ly α line at 2430 Å and other lines in the UV, IR and radio bands, that could provide an other way to observe positron annihilation from astrophysical sources (e.g. Wallyn *et al.* 1996).

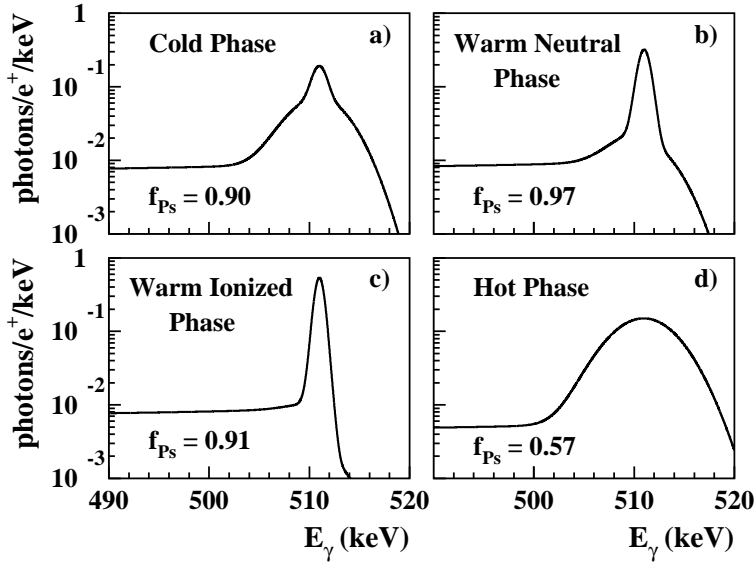


Fig. 16. Calculated gamma-ray spectra of the positron annihilation radiation produced in the various phases of the interstellar medium. Processes involving interstellar dust are not taken into account. The calculations are normalized to one positron annihilation in each phase. f_{Ps} : fraction of positrons that annihilate through Ps formation.

narrower line due to the direct annihilation of 10% of the positrons with bound electrons. In the warm neutral phase (of temperature $T=8000$ K and ionization fraction $\zeta=n_{e^-}/(n_{e^-}+n_H)=0.15$, McKee & Ostriker 1977), the fraction of positrons forming Ps in flight is reduced to 22%. Most of the positrons get thermalized and form Ps by charge exchange just above the energy threshold (6.8 eV in the center of mass for $e^+ + H \rightarrow Ps + p$). The annihilation line has a FWHM of 1.5 keV (Bussard *et al.* 1979). In the warm ionized phase ($T=8000$ K, $\zeta=0.68$), the 511 keV line is even narrower (1.1 keV FWHM), because a significant fraction of thermal positrons form Ps through radiative recombination, which does not have an energy threshold. Finally, in the hot phase of the interstellar medium ($T=4.5 \times 10^5$ K), all the positrons get thermalized and the annihilation line should be broad (≈ 7.4 keV FWHM) due to the thermal motion of the the center of mass of the e^+e^- pairs which annihilate. Crannell *et al.* (1976) estimated the width of the 511 keV line from both para-Ps annihilation following radiative recombination and direct annihilation with free electrons as $\text{FWHM}=11 \times (T/10^6 \text{ K})^{1/2}$ keV. However, the line width could be significantly reduced if annihilation on interstellar dust is important (Guessoum *et al.* 1991). The results shown in Figure 16 are in good agreement with the recent calculations of Dermer & Murphy (2001), except for the cold phase, for which they found the narrow line component from positron annihilation with bound electrons to be negligible.

Harris *et al.* (1998) have measured, with the TGRS instrument (Germanium detector) on the *WIND* spacecraft, the width of the 511 keV line from the Galactic center region to be narrow, $\text{FWHM}=1.81\pm0.54\pm0.14$ keV, and the Ps fraction to be large, $f_{Ps}=0.94\pm0.04$, in good agreement with the most recent OSSE result: $f_{Ps}=0.93\pm0.04$ (Kinzer *et al.* 2001). The narrow line width suggests that most of the positrons can not penetrate deeply into molecular clouds and that annihilation in the hot interstellar phase is not predominant, unless dust grains sprinkled into the hot plasma are important sites of annihilation. However, the Ps fraction would then be very low (<0.5 , Guessoum *et al.* 1991), in conflict with the measured values. Thus, these observations favor a scenario in which the Galactic positrons annihilate predominantly in the warm, partially ionized interstellar medium. The spectroscopic-imaging capability of *INTEGRAL* should allow a better determination of the nature and the spatial distribution of the emitting regions. This would shed new light on the sources of the positrons and on the thermodynamic properties of the annihilation media.

I would like to thank Jean Ballet, Jürgen Kiener, David Lunney and Alexandre Marcowith for critical reading of the manuscript.

References

- Anders, E. and Grevesse, N. 1989, *Geochim. Cosmochim. Acta*, 53, 197
- Angulo, C. *et al.* (The NACRE collaboration) 1999, *Nucl. Phys.*, A656, 3
- Ajzenberg-Selove, F. 1991, *Nucl. Phys.*, A523, 1
- Arnaud, M. and Raymond, J. 1992, *ApJ*, 398, 394
- Arnaud, M. and Rothenflug, R. 1985, *A&AS*, 60, 425
- Bahcall, J. N. and Moeller, C. P. 1969, *ApJ*, 155, 511
- Baring, M. G., Jones, F. C. and Ellison, D. C. 2000, *ApJ*, 528, 776
- Berger, M. J. and Seltzer, S. M. 1982, *Stopping Powers and Ranges of Electrons and Positrons*, National Bureau of Standards report: NBSIR 82-2550, U.S. Dept. of Commerce, Washington, D.C. 20234
- Bhat, M. R. 1998, *Nucl. Data Sheets*, 85, 415
- Bildsten, L., Salpeter, E. E. and Wasserman, I. 1992, *ApJ*, 384, 143
- Bildsten, L., Salpeter, E. E. and Wasserman, I. 1993, *ApJ*, 408, 615
- Bloemen, H. and Bykov, A. M. 1997, *Proc. of the 4th Compton Symposium*, Dermer, C. D., Strickman, M. S., Kurfess, J. D. (eds.), AIP Conf. Proc. 410, p. 249
- Borkowski, K. J., Lyerly, W. J. and Reynolds, S. P. 2001, *ApJ*, 548, 820
- Brown, B. L., Leventhal, M., Mills, A. P., Jr. and Gildey, D. W. 1984, *Phys. Rev. Letters*, 53, 2347
- Bussard, R. W., Ramaty, R. and Drachman, R. J. 1979, *ApJ*, 228, 928
- Bykov, A. M., Bloemen, H., Ivanchik, A. V., Konstantinov, A. N., Krassilchtchikov, A. M. and Lazarev, V. Y. 1999, in *Proc. 3rd INTEGRAL Workshop, The Extreme Universe*, *Astrophys. Lett. & Comm.*, 38, 285
- Cameron, J. A. and Singh, B. 1999, *Nucl. Data Sheets*, 88, 299

- Chan, K.-W. and Lingenfelter, R. 1993, ApJ 405, 614
- Clayton, D. D. 1982, *Essays in Nuclear Astrophysics*, Barnes, C. A., Clayton, D. D. and Schramm, D. N. (eds), (Cambridge: Cambridge University Press)
- Clayton, D. D. 1983, *Principles of Stellar Evolution and Nucleosynthesis* (Chicago and London: The University of Chicago Press)
- Coc, A., Hernanz, M., José, J. and Thibaud, J.-P. 2000, A&A, 357, 561
- Crannell, C. J., Joyce, G., Ramaty, R. and Werntz, C. 1976, ApJ, 210, 582
- Dermer, C. D. and Murphy, R. J. 2001, Proc. of the 4th INTEGRAL Workshop, *Exploring the Gamma-Ray Universe*, (ESA Publication SP-459), p. 115
- Diehl, R. and Timmes, F. X. 1998, PASP, 110, 637
- Dogiel, V. A., Ichimura, A., Inoue, H. and Masai, K. 1998, PASJ, 50, 567
- Ebisawa, K. *et al.* 1996, PASJ, 48, 425
- Ellison, D. C. and Ramaty, R. 1985, ApJ, 298, 400
- Elwert, G. 1952, Z. Naturf. 7a, 432, 703
- Fabian, A. C., Iwasawa, K., Reynolds, C. S. and Young, A. J. 2000, PASP, 112, 1145
- Faurobert, M. 1986, A&A, 158,191
- Ferland, G. *et al.* 1995, *The Analysis of Emission Lines*, ed by Williams, R. and Livio, M., STScI Symposium Series 8, (Cambridge University Press), p. 83
- Firestone, R. B. 1996, *Table of Isotopes*, ed. by Shirley, S. V., (New York: Wiley-Interscience Publication)
- Gabriel, A. H. 1972, MNRAS, 160, 99
- Gabriel, A. H. and Jordan, C. 1969, MNRAS, 145, 241
- Gabriel, A. H. and Phillips, K. J. H. 1979, MNRAS, 189, 319
- Garcia, J. D., Fortner, R. J. and Kavanagh, T. M. 1973, Rev. Mod. Phys., 45, 111
- Groom, D. E. *et al.* (Particle Data Group) 2000, Eur. Phys. Jour., C15, 1 and 2001 partial update for edition 2002 (URL: <http://pdg.lbl.gov>)
- Guessoum, N. 1989, ApJ, 345, 363
- Guessoum, N. and Gould, R. J. 1989, ApJ, 345, 356
- Guessoum, N., Ramaty, R. and Lingenfelter, R. E. 1991, ApJ, 378, 170
- Guessoum, N., Skibo, J. G. and Ramaty, R. 1997, Proc. of the 2nd INTEGRAL Workshop, *The Transparent Universe*, (ESA Publication SP-382), p. 113
- Halpern, J. P. and Grindlay, J. E. 1980, ApJ, 242, 1041
- Harra-Murnion, L. K. *et al.* 1996, A&A, 306, 670
- Harris, M. J., Teegarden, B. J., Cline, T. L., Gehrels, N., Plamer, D. M., Ramaty, R. and Seifert, H. 1998, ApJ, 501, L55
- Hernanz, M., Gómez-Gomar, J., José, J. and Coc, A. 2001, Proc. of the 4th INTEGRAL Workshop, *Exploring the Gamma-Ray Universe*, (ESA Publication SP-459), p. 65
- Higdon, J. C. and Lingenfelter, R. E. 1977, ApJ, 215, L53
- Hoffmann, D. H. H., Brendel, C., Genz, H., Löw, W., Müller, S. and Richter A. 1979, Z. Phys A, 293, 187
- Horsley, A. 1966, Nucl. Data, A2, 243
- Hua, X.-M. and Lingenfelter, R. E. 1987a, Solar Phys., 107, 351
- Hua, X.-M. and Lingenfelter, R. E. 1987b, ApJ, 319, 555

- Iyudin, A. F. *et al.* 2002, to be published in Proc. of Baltimore Gamma Ray Symp. (AIP Conf. Series)
- Jean, P. and Guessoum, N. 2001, *A&A*, 378, 509
- Junde, H. 1999, *Nucl. Data Sheets*, 86, 315
- Kaastra, J. S. and Mewe, R. 1993, *A&AS*, 97, 443
- Kaastra, J. S., Mewe, R. and Nieuwenhuijzen, H. 1996, in *UV and X-ray Spectroscopy of Astrophysical and Laboratory Plasmas*, ed. by Yamashita, K. and Watanabe, T. (Tokyo: Universal Academy Press), p. 411
- Kallman, T. and Bautista, M. 2001, *ApJS*, 133, 221
- Kallman, T. R. and McCray, R. 1982, *ApJS*, 50, 263
- Kiener, J., de Séréville, N. and Tatischeff, V. 2001, *Phys. Rev. C*, 64, 25803
- King, M. M. 1993, *Nucl. Data Sheets*, 69, 1
- Kingdon, J. B. and Ferland, G. J. 1996, *ApJS*, 106, 205
- Kingdon, J. B. and Ferland, G. J. 1999, *ApJ*, 516, L107
- Kinzer, R. L., Milne, P. A., Kurfess, J. D., Strickman, M. S. Johnson, W. N. and Purcell, W. R. 2001, *ApJ*, 559, 282
- Koch, H. W. and Motz, J. W. 1959, *Rev. Mod. Phys.*, 31, 920
- Kozlovsky, B. and Ramaty, R. 1974, *ApJ*, 191, L43
- Kozlovsky, B., Lingenfelter, R. E. and Ramaty, R. 1987, *ApJ*, 316, 801
- Kozlovsky, B., Murphy, R. J. and Ramaty, R. 2002, in preparation
- Krause, M. O. 1979, *J. Phys. Chem. Ref. Data*, 8, 307
- Laming, J. M. 2002, to be published in Proc. of the Joint SOHO-ACE Workshop, *Solar and Galactic Composition*, (AIP Conf. Series)
- Landi, E., Landini, M., Dere, K. P., Young, P. R. and Mason, H. E. 1999, *A&AS*, 135, 339
- Leising, M. D. 2001, *ApJ* 563, 185
- Liedahl, D. A. 1999, in *X-ray Spectroscopy in Astrophysics*, ed. by van Paradijs, J. and Bleecker, J. A. M. (Berlin: Springer-Verlag), p. 189
- Liedahl, D. A., Kahn, S. M., Osterheld, A. L. and Goldstein, W. H. 1990, *ApJ*, 350, L37
- Lingenfelter, R. E. and Ramaty, R. 1977, *ApJ*, 211, L19
- Lisse, C. M., Christian, D. J., Dennerl, K., Meech, K. J., Petre, R., Weaver, H. A. and Wolk, S. J. 2001, *Science*, 292, 1343
- Long, X., Liu, M., Ho, F. and Peng, X. 1990, *At. Data Nucl. Data Tables*, 45, 353
- McConnell, M., *et al.* 1997, Proc. of the 4th Compton Symposium, Dermer, C. D., Strickman, M. S., Kurfess, J. D. (eds), AIP Conf. Proc. 410, p. 1099
- McKee, C. F. and Ostriker, J. P. 1977, *ApJ*, 218, 148
- Mewe, R., Lemen, J. R. and van den Oord, G. H. J. 1986, *A&AS*, 65, 511
- Mewe, R. 1999, in *X-ray Spectroscopy in Astrophysics*, ed. by van Paradijs, J. and Bleecker, J. A. M. (Berlin: Springer-Verlag), p. 109
- Meyer, J. P. 1972, *A&AS*, 7, 417
- Milne, E. A. 1924, *Philos. Mag. J. Sci.*, 47, 209
- Milne, P. A., Kurfess, J. D., Kinzer, R. L. and Leising, M. D. 2002, to be published in Proc. of the Workshop *Astronomy with Radioactivities III*, *New Astronomy Reviews*

- Mochizuki, Y., Takahashi, K. Janka, H.-Th., Hillebrandt, W. and Diehl, R. 1999, A&A, 346, 831
- Morrison, R. and McCammon, D. 1983, ApJ, 270, 119
- Murphy, R. J., Dermer, C. D. and Ramaty, R. 1987, ApJS, 63, 721
- Ore, A. and Powell, J. L. 1949, Phys. Rev., 75, 1696
- Porquet, D. and Dubau 2000, J. A&AS, 143, 495
- Porquet, D., Arnaud, M. and Decourchelle A. 2001a, A&A, 373, 1110
- Porquet, D., Mewe, R., Dubau, J., Raassen, A. J. J. and Kaastra, J. S. 2001b, A&A, 376, 1113
- Prantzos, N. 1999, in Proc. 3rd INTEGRAL Workshop, *The Extreme Universe*, Astrophys. Lett. & Comm., 38, 337
- Quarles, C. A. 1976, Phys. Rev. A, 13, 1278
- Rajagopal, M. and Romani, R. W. 1996, ApJ, 461, 327
- Ramaty, R., Kozlovsky, B. and Lingenfelter, R. E. 1975, Space Sci. Rev., 18, 341
- Ramaty, R., Kozlovsky, B. and Lingenfelter, R. E. 1979, ApJS, 40, 487
- Ramaty, R., Kozlovsky, B. and Lingenfelter, R. E. 1996, ApJ, 456, 525
- Ramaty, R. and Lingenfelter, R. E. 1979, Nature, 278, 127
- Ramaty, R. and Mandzhavidze, N. 2000, in *Highly Energetic Physical Processes and Mechanisms for Emission from Astrophysical Plasmas*, ed. by Martens, P. C. H., Tsuruta, S. and Weber, M. A. (San Francisco: Astron. Soc. Pacific), p. 123
- Raymond, J. C. 1988, in *Hot Thin Plasmas in Astrophysics*, ed. by Pallavicini, R. (Dordrecht: Kluwer Acad. Publ.), p. 3
- Ross, R. R. 1979, ApJ, 233, 334
- Rybicki, G. B. and Lightman, A. P. 1979, *Radiative Processes in Astrophysics* (New York: Wiley)
- Sako, M., Liedahl, D. A., Kahn, S. M. and Paerels, F. 1999, ApJ, 525, 921
- Savage B. D., Sembach K. R. 1996, ARA&A, 34, 279
- Schönfelder, V., *et al.* 2000, A&AS, 143, 145
- Share, G. H. and Murphy, R. J. 2001, in Proc. of the GAMMA 2001 Symposium, AIP Conf. Proc. 587, p. 603
- Shull, J. M. 1979, ApJ, 234, 761
- Shvartsman, V. F. 1972, Astrophysics, 6, 56
- Smith, R. K., Brickhouse, N. S., Liedahl, D. A. and Raymond, J. C. 2001, ApJ, 556, L91
- Sobelman, I. I. 1979, *Atomic Spectra and Radiative Transitions*, (Berlin: Springer-Verlag)
- Stecker, F. 1969, Ap&SS, 3, 479
- Tatischeff, V., Ramaty, R. and Kozlovsky, B. 1998, ApJ, 504, 874
- Tatischeff, V. and Ramaty, R. 1999, in Proc. 3rd INTEGRAL Workshop, *The Extreme Universe*, Astrophys. Lett. & Comm., 38, 465
- Tatischeff, V., Thibaud, J.-P., Kiener, J., Cassé, M. and Vangioni-Flam, E. 2001, Proc. of the 4th INTEGRAL Workshop, *Exploring the Gamma-Ray Universe*, (ESA Publication SP-459), p. 105
- Timmes, F. X. and Woosley, S. E. 1997, ApJ, 481, L81
- Valinia, A., Tatischeff, V., Arnaud, K., Ebisawa, K. and Ramaty, R. 2000, ApJ, 543, 733

- Verner, D. A., Yakovlev, D. G., Band, I. M. and Trzhaskovskaya, M. B. 1993, *At. Data Nucl. Data Tables*, 55, 233
- Vestrand, W. T., Share, G. H., Murphy, R. J., Forrest, D. J., Rieger, E., Chupp, E. L. and Kanbach, G. 1999, *ApJS*, 120, 409
- Wallyn, P., Mahomey, W. A., Durouchoux, Ph. and Chapuis, C. 1996, *ApJ*, 465, 473
- Wang, H. T. and Ramaty, R. 1974, *Solar Phys.*, 36, 129
- Weisheit, J. C. 1974, *ApJ*, 190, 735
- Weisskopf, M. C., Brinkman, B., Canizares, C., Garmire, G., Murray, S. and Van Speybroeck, L. P. 2002, *PASP*, 114, 1
- Younger, S. M. 1982, *Phys. Rev.*, A26, 3177
- Zarro, D. M., Dennis, B. R. and Slater, G. L. 1992, *ApJ*, 391, 865
- Zobel, W., Maienschein, F. C., Todd, J. H. and Chapman, G. T. 1968, *Nucl. Sci. Eng.*, 32, 392
- Zurek, W. H. 1985, *ApJ*, 289, 603